Master's thesis

NTNU
Norwegian University of Science and Technology
Faculty of Natural Sciences
Department of Physics

Karina Brunstøl

# Characterization of Multicellular Spheroids for Drug Delivery Studies

Master's thesis in Applied Physics and Mathematics
Supervisor: Catharina de Lange Davies
Co-supervisor: Caroline Einen
July 2023

NTNU
Norwegian University of
Science and Technology

Karina Brunstøl

# Characterization of Multicellular Spheroids for Drug Delivery Studies

Master's thesis in Applied Physics and Mathematics
Supervisor: Catharina de Lange Davies
Co-supervisor: Caroline Einen
July 2023

Norwegian University of Science and Technology
Faculty of Natural Sciences
Department of Physics

NTNU
Norwegian University of
Science and Technology

# Preface

This master thesis concludes my Master of Science degree in Applied Physics and Mathematics, with specialization in Biophysics and Medical Technology, at the Norwegian University of Science and Technology (NTNU). This thesis builds upon the author's specialization project carried out in the fall of 2022, and consequently there are some overlaps in the sections *Theory* and *Methods and Materials*.

I would like to express my sincere gratitude to my supervisor and co-supervisor Catharina de Lange Davies and Caroline Einen for their guidance, expertise and valuable feedback. I would also like to thank head engineer Sylvie Lelu for training and patience in the cell lab, and senior engineer Astrid Bjørkøy for microscope traning and providing the Matlab script used for nanoparticle uptake analysis. I also would like to thank the entire biophysics research group for your inclusiveness as well as good discussions. Your enthusiasm for your work is really inspiring. Furthermore I want to thank my good friends and classmates for your friendship, support and good times over the last five years. The long days (and nights) studying would not be the same without you. Lastly, I want to thank my family for always being proud of me, despite never remembering exactly what I am studying.

Karina Brunstøl

Trondheim, July 2023

## Abstract

Multicellular spheroids (MCSs) are 3D tumor models that, by better emulating the tumor microenvironment (TME), can improve in-vitro cancer research, with the aim to reduce reliance on in-vivo experiments.

*Purpose:* To characterize MCSs from three different tumor cell lines from mice, in terms of growth characteristics, extracellular matrix (ECM) contents, and nanoparticle (NP) uptake. The objective was to gain insight into their potential as in-vitro models for drug delivery studies alongside murine experiments.

*Methods and Materials:* The tumor cell lines (4T1, CT26, and KPC) were cocultured as MCSs with fibroblast NIH/3T3 using both the liquid overlay method, and the nonadhesive hydrogel micro-molds method. Growth characteristics of the cells in monolayer were studied by measuring the doubling times (DTs) and assessing the morphologies using phase contrast microscopy. MCSs were cultivated in parallel in the growth medium of the TCs (TC-GM) and the fibroblasts (F-GM), and volume and sphericity were measured. To visualize the organization of TCs and fibroblasts within the MCSs the different cells were fluorescently labeled and images using confocal laser scanning microscopy (CLSM). ECM constituents contents, collagen and sGAG, were measured using enzymatic extraction followed by absorbance measurements. Lastly, NP uptake was studied with CLSM imaging of the MCSs at 50 µm depth followed by data analysis using a Matlab script.

*Results:* CT26 MCSs exhibited significantly larger size and sphericity than the other spheroid models. 4T1 MCSs showed intermediate characteristics, while KPC MCSs were the smallest with the lowest sphericity. The CT26 MCSs obtained larger volumes when cultivated in TC-GM than F-GM, while for KPC MCSs the opposite was observed. Cellular organization varied, with 4T1 and CT26 mixed with the fibroblasts and formed heterospheroids, with variation in homogeneity, while KPC exhibiting complete separation of cell types. NP penetration was limited in, primarily accumulating in the first cell layer, with smaller NPs showing better penetration. Collagen levels were very low, below detection limit, while sGAG contents were notably higher. No difference in contents was found between the MCSs, and ECM contents can not explain differences in NP uptake. The observed differences in cellular organization is suggested to be due to differences in cell-cell interactions and cadherin expression, and is though to possibly have an effect on uptake.

*Conclusion:* Differences between the three different spheroid models was found, which makes them interesting candidates for further drug delivery studies. With further investigation, eventually we could get more insight into whether these distinctions reflect the properties of in-vivo tumor models.

## Sammendrag

Multicellulære sfæroider (MCSer) er 3D-tumormodeller som ved å bedre etterligne tumor-mikromiljøet (TME) kan forbedre in vitro-kreftforskning med mål om å redusere behovet for dyreforsøk.

*Formål:* Å karakterisere MCSer fra tre forskjellige tumortcellelinjer fra mus med tanke på vekstegenskaper, innhold av ekstracellulær matriks (ECM) og nanopartikkelopptak. Målet var å få innsikt i deres potensial som in vitro-modeller for studier av legemiddellevering i kombinasjon med murine eksperimenter.

*Metoder og materiale:* kreftcellelinjene (4T1, CT26 og KPC) ble kultivert som MCSer sammen med fibroblastene NIH/3T3 ved bruk av to ulike produksjonsmetoder. Vekstegenskapene til cellene i monolag ble studert ved å måle doblingstiden (DT) og vurdere morfologien ved bruk av fasekontrastmikroskopi. MCSer ble dyrket parallelt i vekstmediet til kreftcellene (TC-GM) og fibroblastene (F-GM), og volum og sfærisitet ble målt. For å visualisere organisasjonen av TCene og fibroblastene innenfor MCSs, ble de forskjellige cellene fluorescerende merket, og bilder ble tatt ved hjelp av konfokal laserskanningmikroskopi (CLSM). Innholdet av ECM-komponentene kollagen og sGAG ble målt ved hjelp av enzymatisk ekstraksjon etterfulgt av absorbansmålinger. Til slutt ble NP-opptak studert ved CLSM-avbildning av MCSs etterfulgt av dataanalyse ved hjelp av et Matlab-skript.

*Resultater:* CT26 MCSer viste betydelig større volum og sfærisitet enn de andre sfæroide-modellene. 4T1 MCSer viste middels egenskaper, mens KPC MCSer var både minst og med lavest sfærisitet. CT26 MCSer oppnådde større volum når de ble dyrket i TC-GM sammenlignet med F-GM, mens det motsatte ble observert for KPC MCSer. Celleorganisasjonen varierte, der 4T1 og CT26 ble blandet med fibroblastene og dannet heterosfæroider, men med ulik grad av homogenitet. KPC derimot viste fullstendig separasjon av cellepopulasjonene. NP-penetrasjonen var begrenset og akkumulertes hovedsakelig i det første cellelaget. Mindre NPer ga bedre penetrasjon. Kollagennivåene var svært lave og under deteksjonssgrensen, mens sGAG-innholdet var betydelig høyere. Det ble ikke funnet noen signifikante forskjeller mellom ECM-innholdet i MCSene, og dermed kan ikke dette brukes til å forskjellene i NP-opptak. De observerte forskjellene i celleorganisasjon antydes å skyldes forskjeller i celle-celle-interaksjoner og uttrykkelse av cadheriner, og dette foreslås å være en påvirkende faktor til forskjellene i NP-opptaket.

*Konklusjon:* Det ble funnet forskjeller mellom de tre forskjellige sfæroide-modellene, noe som gjør dem til interessante kandidater for videre studier av legemiddellevering. Med ytterligere undersøkelser vil vi etter hvert kunne få mer innsikt i om disse forskjellene gjenspeiler egenskapene til tilsvarende in vivo-tumor modeller.

## Abbreviations

**CAF** Cancer Associated Fibroblasts

**CAM** Cell Adhesion Molecule

**CI** Confidence Interval

**CLSM** Confocal Laser Scanning Microscopy

**DT** Doubling Time

**ECM** Extra Cellular Matrix

**EMT** Epithelial-Mesenchymal-Transition

**EPR** Enhanced Permeability and Retention

**F-GM** Fibroblast-Growth Medium

**FBS** Fetal Bovine Serum

**GAG** Glycosaminoglycans

**MCS** Multicellular Spheroid

**NAF** Normal-tissue Associated Fibroblasts

**NP** Nanoparticle

**PBS** Phosphate Buffered Saline

**ROI** Region of Interest

**TC** Tumor Cell

**TC-GM** Tumor Cell-Growth Medium

**TME** Tumor Microenvironment

**SD** Standard Deviation

**sGAG** sulfated Glycosaminoglycans

**SHG** Second Harmonic Generation

**V-DT** Volume-Doubling Time

**WHO** World Health Organization

# Table of Contents

# Chapter 1

# Introduction

### Motivation

Cancer is one of the leading causes of deaths, accounting for almost 10 million deaths worldwide in 2020 [1]. The number of incidences globally are expected to increase by about 70% over the next 20 years according to the World Health Organization (WHO).

One of the biggest limitations of effective cancer treatment when using chemotherapeutic drugs is the damage to healthy tissues and cells, and the side effects this entails. This is caused by the non-selective nature of the drugs, and when injecting chemotherapeutic agents only around 0.01% of the drugs will reach the tumor site [2]. A possible solution to fix the problem of low and heterogeneous uptake is to encapsulate the drug in nanoparticles (NPs). By increasing the size of the drug, the uptake to healthy cells decreases, as the epithelial cells are tightly bound in healthy blood vessels. The poorly-organized endothelial barriers of fast-growing tumors lead to large openings which permit selective uptake of particles of larger size [3]. However cancer-associated fibroblasts (CAFs) can produce a very dense extracellular matrix (ECM), limiting the penetration of NPs into the deeper layers of the tumor.

To develop nanoparticles and drug delivery systems for cancer therapy, they should be studied using relevant disease models. As it is important to do research in as similar conditions as possible as in human tumors, in-vivo experiments in mice are heavily used for drug delivery studies and research on the mechanisms of delivery into tumors. Finding a method to conduct in-vitro lab experiments with comparable results is of importance to reduce the cost and accessibility of further research, as well as reducing the need for animal use.

Compared to 2D in-vitro cell monolayers, 3D cell culture models, such as multicellular spheroids (MCSs), provides a closer mimicry of in-vivo conditions. This is achieved through enhanced cell-to-cell contact and ECM production. Additionally it is possible to cultivate spheroids with ECM-producing fibroblasts to further emulate the in-vivo conditions, while still maintaining the controlled environment of an in-vitro study.

Research has shown that due to the formation of ECM, certain cancer treatments are less effective in 3D multicellular spheroids compared to 2D monolayer cultures, which makes them suitable candidates for drug delivery studies [3].

### Aims of study

The objective of this master thesis was to characterize MCSs formed by different murine cancer cell lines, namely 4T1, CT26, and KPC, in combination with fibroblasts NIH/3T3. The aim was to identify similarities and differences among these spheroid models. Specifically, the study aimed to investigate the growth patterns, cellular distribution and ECM composition of the MCSs, and examine their impact on NP uptake and penetration into the spheroids.

To reach these goals, a number of investigation methods was used:

1. Investigate cell growth of the various cell lines in both monolayer and as MCSs.
2. Determine the cellular organization of fibroblasts and TCs within MCSs using confocal laser scanning microscopy (CLSM).
3. Measure collagen and sGAG contents within the various MCSs using enzymatic extraction and absorbance measurements.
4. Measuring NP uptake into the MCSs at different time points using CLSM, using two different sized NPs, and explore correlation between uptake and the other objectives mentioned above.

The thesis is also a continuation of the author's specialization project [4] concerning MCSs using 4T1 and CT26, where different methods for cultivation were tested and optimized, and the first look into the distribution of fibroblast within MCSs was done. Parts of the theory and method sections in this thesis is reused or adapted from this project.

# Chapter 2

# Theory

## 2.1 Cancer development

Cancer is a group of diseases that can occur in any tissue of the body, and is characterized by abnormal cell growth and division [5]. Normal cells have numerous mechanisms that controls DNA repair, cell growth, division. If genetic mutations occur that are able to escapes and disrupts these mechanisms, it can lead to the formation of a tumor. Benign tumors are non-cancerous and are usually confined within the tissue in which it arise which makes them generally not life-threatening. On the other hand, if the tumor acquire the potential to invade surrounding tissue and metastasize to other parts of the body it is malignant [3]. While cancer is a disease usually associated with malignant tumors only, it will in this thesis not be differentiated between benign and malignant tumors. The terms "cancer" and "tumor" will therefore be used interchangeably.

#### The Hallmarks of Cancer

The complexity of diversity of cancer can makes it difficult to comprehend, and the more research is done, the more unknowns are uncovered. In efforts to gather information and simplify the problem, Hanahan and Weinberg released in 2000 a list of six alterations in the cell physiology that is essential in the transformation of normal cells into malignant cancers [6]. They proposed that most cancers, if not all, acquire this set of functional traits during their development that breaks the innate anticancer defense mechanism of healthy cells and tissues and collectively leads to cancer development.

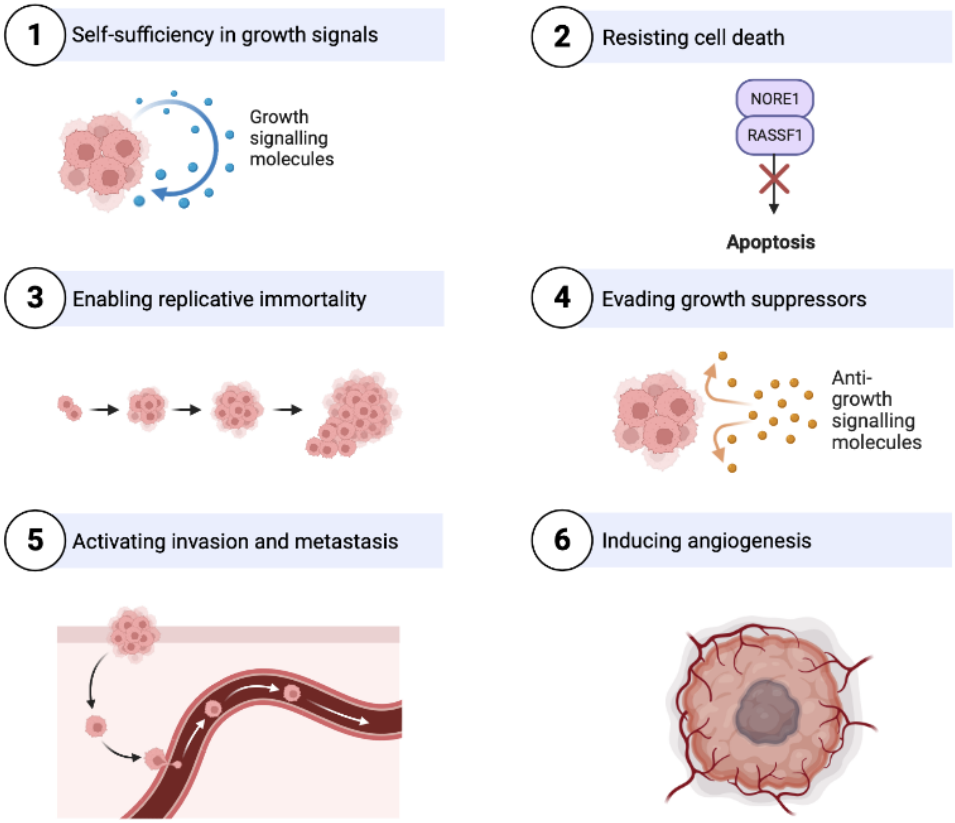


**Figure 2.1:** The 6 original hallmarks of cancer from 2000. Created with BioRender.com

The abnormal and rapid growth and proliferation of TCs are summarized in items 1-4 in Figure 2.1. Normal cells are dependent on mitogenic growth signals to transform from a quiescent state into an active, proliferative one. On the contrary, TCs have acquired the capability of generating some of their own growth signals (1) and therefore become increase their independence on their environment. With the additional abilities to avoid both antigrowth signals (4) and apoptosis (2) this results in replicative immortality (3).

Uncontrolled growth means increased need for nutrients, and cells within unusual proliferative lesions acquire angiogenic capabilities. This means they are able to induce their own vasculature, allowing them to grow even larger in size. The next step in the development is invasion into adjacent tissues, extravasation into blood vessels, and eventually metastasis to distant sites. Although most of the circulating TCs does not survive the journey through the blood- and lymphatic system, some cells are able to overcome all the barriers and adapt to the microenviroment at the new site. Successful establishment of a metastatic tumors are associated with poorer prognosis for the patients.

In both 2011, and 2022 they expanded the list with two emerging hallmarks and two characteristics that enables tumorigenesis and cancer growth [7]. With these new additions they acknowledged that tumors are more than proliferating TCs, and focused

more on the effect of the tumor microenvironment (TME).

## 2.2 Tumor Microenvironment

The previous section described the necessary properties cells need to adapt in order for tumor development to occur. A tumor however, does not only consist of cancer cells, but is rather a complex The complex environment surrounding a tumor is called the TME which plays a crucial role in the growth, migration, and invasion of the tumor. TME is also called tumor stroma and consists of non-malignant components in the vicinity of the cancer cells. The TME includes cellular parts like endothelial, mesenchymal (e.g fibroblast), and immune cells together with non-cellular parts like the ECM and the vasculature [8] [9].

The tumor stroma has shown increased resistance to cancer therapy and is one possible target in cancer therapy. The ability of MCSs to replicate the complexity of TME is the reason why they have been and are still attracting so much attention on the road to closing the gap between in-vivo and in-vitro animal models.

### 2.2.1 Tumor associated ECM

The ECM is the large network of proteins and glycosaminoglycans (GAGs) Generally, we divide the ECM into two subgroups with slightly different composition and structure: the basal membrane and the interstitial matrix [10] [11]. Polysaccharides and fibrous proteins in the form of gels, fill the interstitial space, and provide a cushion against the stress placed on the extracellular matrix. Additionally, basement membranes are sheet-like layers of ECM that support various epithelial cells.

The ECM components all have different physical and biochemical properties, giving the ECM a wide range of functions. For a long time the ECM was considered to mainly have structural and supportive mechanisms, but the ECM is now recognized to be involved in virtually all cell behaviours either directly or indirectly [11]. Some of the activities the ECM plays an important part in, other than providing structure, is maintaining homeostasis and cell proliferation and differentiation.

Highly dynamic properties have been established for the ECM as it is constantly being remodeled to adjust to the specific needs in different tissues and organs [12]. Modifications can be done by changing either the composition or amount of ECM, or the spatial organization of the components. It is the cells that secrete and remodel the surrounding ECM, but the ECM can in turn regulate the cells behaviour and activity. We say that cell-ECM interactions are reciprocal and this is what enables cells to quickly adapt to changes in environment [11].

The components with the most importance in this thesis is sulfated glycoosaminoglycans

(sGAG) and collagen.

### Proteocglycans

GAGs are carbohydrate polymers that are typically attached to extracellular matrix proteins to form proteoglycans [13]. The proteoglycan is hydrophilic and has a net negative charge. This attracts both water and cations, thus proteoglycans keeps the ECM and the cells within it hydrated. Proteoglycans may also be capable of trapping and storing growth factors in the ECM [10].

There are five different GAGs, where four of them are sulfated glycosaminoglycans. This group includes chondroitin sulfate, keratan sulfate, dermatan sulfate, and heparan sulfate [10]. Hyaluronic acid is the last GAG and is different from the others as it is not found as a proteoglycan, but rather free in the extracellular space, where it resists compression by absorbing water.

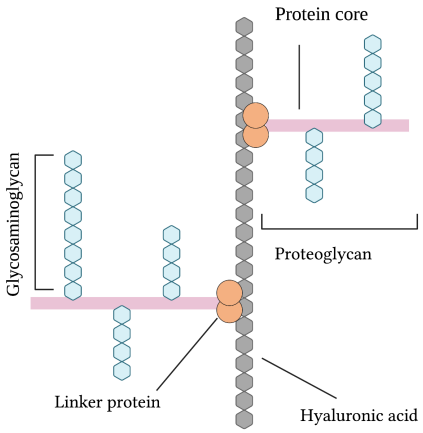


**Figure 2.2:** Proteoglycan complex structure. Created in Biorender.com

### Collagen

The most abundant protein in the ECM is collagen [11][10]. The family of collagens are characterized by the type of structure they form, i.e collagen I + II which is a fibrillar type and collagen IV that is found in the basement membrane. All of them share the same feature of being composed of three strands of amino acids, termed $\alpha$ chains, that form a triple helix, called the collagen molecule. These molecules self-assemble into collagen fibrils and then further into collagen fibers, as seen in Figure 2.3. The results are strong, flexible fibers that increases the tensil strength in tissues, as well as providing structure.

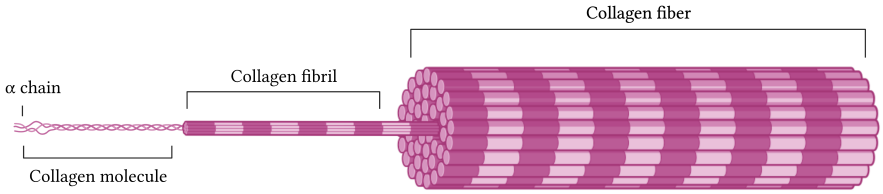


**Figure 2.3:** Structure of collagen fibers, consisting of collagen fibrils, collagen molecules and $\alpha$ chains. Created in Biorender.com

### 2.2.2 Fibroblasts

One of the most important ECM-producing cells are fibroblasts, and are normally found as a heterogeneous population located in the interstitium of all normal tissues and organs [10]. In normal, healthy stroma, a small number of fibroblasts are usually found ingrained in the ECM. They are generally found as single cells in a quiescent state, usually with negligeble metabolic and transciptic activity. They are highly plastic cells and are able to survive severe stress in highly damaged and dynamic environments [8].

These quiescent fibroblasts inhibit the ability to respond to growth factors and in turn become activated, although the mechanisms behind this activation are not yet fully understood. The activation of fibroblasts was first observed as a wound healing response to damage in healthy tissue. There are assumed to be two separate types of activation; 'reversible' and 'inversible' for normal-tissue associated fibroblasts (NAFs) and cancer-associated fibroblasts (CAFs) respectively[8].

The activation of NAFs can be triggered from different stimuli including stress, hypoxic conditions, growth factors like TGF$\beta$ or chemokines and cytokines. This leads to increased expressions of certain proteins that can induce contractile properties of the cells by enhanced ECM production, cytockeletal remodelling, and a shape-shift. Subsequently, epigenetic changes can induce the irreversible activation of CAFs.

CAF is a collective term that covers all of the heterogenous population of irreversibly activated fibroblasts with various functions [8]. They commonly have been identified due to their expression of various CAF-markers [14]. The continous emergence and accumulation of malignent cells in the TME corresponds to an ongoing tissue injury. Appropriately tumors are considered 'wounds that do not heal', and studies have suggested that cancer cells recruit CAFs in similar manner as NAFs are in wound healing [15] [8].

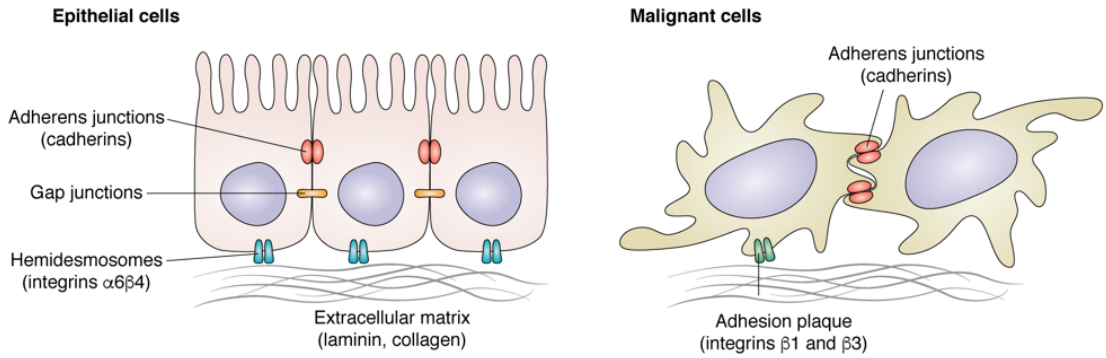


**Figure 2.4:** Illustation of some important cell adhesion molecules and cell junctions, and how they organize in epithelial vs malignant cells. Figure from [5].

## 2.3 Cell Adhesion

Cell Adhesion Molecules (CAMs) are cell surface proteins that mediate both cell-cell and cell-matrix interactions. There are four major families of CAMS: cadherins, integrins, selectins and immunoglobin like adhesion molecules [16]. Most of all CAMs are transmembrane proteins with a cytoplasmic, transmembrane, and extracellular domain. With the extracellular domain they can mediate adhesive interactions both between equal cell types (homotypic adhesion) and different cell types (heterotypic adhesion). In addition, they can form homophilic bindings by binding to the same kind of CAM on neighboring cell, or heterophilic binding by binding to a different type of CAM. They can be distributed along the whole contact area, or clustered in specific spots called cell-junctions illustrated in Figure 2.4. This figure also shows the difference of how cell-junctions typically is configurated between healthy epithelial cells and in malignant cells.

### 2.3.1 Cytoskeleton

The cytoskeleton is a network of filaments in cells that gives support and structure to the cell, and is also important in cell adhesion. In eukaryotic cells there are three types of filaments in this network: microtubules, intermediate filaments and microfilaments. Microfilaments are made of linked actin monomers, and are therefore also known as actin filaments [5]. They are usually assembled in two types of structures, bundles and networks. Actin bundles are packed closely and linked parallel, while in networks the actin filaments are loosely linked orthogonal to each other, to create a three-dimensional grid. Stress fibres are cross-linked actin filaments in bundles with myosin motor proteins found in non-muscular cells. The motor proteins allow for contractility, which allow stress fibers to provide force to multiple processes in the cell like adhesion, migration and morphogenesis. Stress fibers constantly assemble and disassemble, and, and can modify in response to outer forces, like mechanical stress [16].

### 2.3.2 Cell-cell interaction and cadherins

Cell-cell adhesions usually involve two different types of interactions. Firstly they form cis-interactions where two CAMS on the same cell combine their extracellular domains and form dimers of oligomers of higher orders. Secondly, trans-interactions are made by CAM oligomers on one cell binding to the CAMs on an adjacent cell [16].

Cadherins are the most important molecules when it comes to cell-cell adhesion. As their name suggest, the functions of cadherins are reliant on the presence of extracellular Ca2+. There are many types of cadherins, but the most extensively expressed ones are the classical E-, P-, and N-cadherins. The expression patterns of cadherin proteins play a crucial role in the biology of epithelial tissues and epithelium-derived cancer cells. In normal epithelial tissues, the presence of E-cadherin is widespread, facilitating cell-cell adhesion and maintenance of tissue integrity [17]. However, certain cancer cells derived from epithelial tissues exhibit a loss of E-cadherin expression, as evidenced by various studies [18][19][20]. In contrast, N-cadherin, which is typically expressed by mesenchymal cells, has been found to be inappropriately expressed by certain cancer cells. This abnormal expression of N-cadherin is associated with increased motility and invasive potential of these cancer cells, as demonstrated in several studies [21] [20]. Due to the relation with epithelial- and mesenchymal to E-cadherin and N-cadherin expression, these two types of cadherin are commonly used as Epitelial-Mesenchymal-Transition (EMT) markers [17][22].

### 2.3.3 Cell-matrix interaction and integrins

As seen in Figure 2.4 adhesion of adjacent cells can also be achieved by cell-matrix interactions like hemidesmosomes. These interactions are essential for cell migration, tissue organization and differentiation [23]. The integrin family is the CAMs most often involved in these interactions, and are heterodimeric integral membrane proteins composed of $\alpha$- and $\beta$-subunits. A single $\beta$ chain can interact with multiple $\alpha$ chains and form various integrins with affinity for different ligands. While integrins on one end binds to different components in the ECM, depending on the composition of $\alpha$-subunits, they also at the at the cytosolic end link to adapter proteins that further bind the cytoskeleton. Individual integrins typically have low affinity for their associated ligands, which is important for cell migration, but the high amount of bindings occurring simultaneously allows tight attachment.

## 2.4 Drug delivery Systems

Cancer treatment strategies, as well as their success rate, strongly depend on the location and stage of the cancer. Common strategies include radiation, chemotherapy and surgery, which may be used individually or in combination for improved outcomes [24].

The non-selective nature of chemotherapeutic drugs result a large amount of healthy cells being affected, and leads to many side effects which again limits the maximum dose and frequency of treatment that the patient can handle [25][2]. Focusing on targeted drug delivery is important to increase the arrival of drug to the wanted area and minimize side effects. Possible mechanisms for this can be enzyme mediation, pH-dependent release, receptor targeting and, use of special vehicles or carriers [26].

Nanoparticles are one of the carrier options available for targeted delivery, and NP drug delivery systems offer the flexibility to tailor their properties to suit specific targets and drug requirements. The size, shape and composition of the nanocarriers can be adjusted accordingly [27]. The size of the particles range from a few nm to several hundred nm in size, and they can be composed of different materials, for example polymers, lipids, dendrimers or metals. In addition, a variation of surface modifications can be applied, as seen in Figure 2.5, by the addition of various molecules of varying properties, for example proteins, targeting ligands, or polyethylene glycolyation (PEGylation) [28]. The targeted NP and drug delivery process can be both active and passive. Passive delivery entails the transport of NP through the permeable blood vessels of tumors, allowing them to diffuse passively into the tumor interstitium and cells. In active targeting the surface of the nanoparticles are modified in such a manner that they identify and bind to specific molecular targets found at the target cell site.

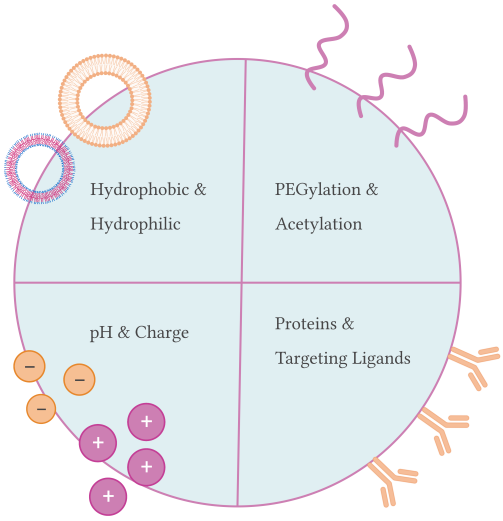


**Figure 2.5:** Surface modifications for nanoparticles. Inspired by [28] and created in Biorender.com

### 2.4.1 Barriers of Drug Delivery

The injected NP and drug particles undergoes a long journey before reaching the tumor cells, and on the way a lot of barriers need to be overcome. The barriers can be divided

into four categories: vascular transport into the tumor, transportation across the blood vessel wall, transportation through the interstitial space and cellular uptake.

#### Vascular Transport

Upon entering the vascular system, NPs face the initial challenge of evading opsonization, where they are recognized and cleared from the body. This can be overcome with some of the modifications mentioned in Figure 2.5, such as PEGylation or creating a hydrophilic surface. Poorly vascularized tumors pose an additional difficulty for NP delivery. Next step is permeating the blood vessels and reach the interstitial space. The small size of drug particles cause them to permeate both healthy and cancerous blood vessels, while the larger size of NPs lead to selective uptake only through the large openings in the vasculature of fast-growing tumors.

#### ECM as a barrier

After successfull transport over the blood vessel walls there is still many barriers that limit the penetration of nanoparticles and drug molecules deeper into the tumor tissues. The dense and overexpressed ECM due to continuous activation of CAFs, functions as physical barrier and leads to low diffusion rate throughout the tumor tissue.

Various cells and other components present in the ECM also forces the drug molecules to follow a non-linear path, further elongating the travel [29]. Additionally, there is a high interstitial pressure, especially in the centre of the tumor, that limits the inward flux of molecules. On the contrary, tumors lack well-defined lymphatic networks which leads to extended retention times in the interstitium for the NPs that comes that far. This is called the enhanced permeability and retention (EPR) effect and promotes drug accumulation within tumors [30].

#### Cellular Uptake

For the most effective drug delivery, the NPs should preferably enter the cell and release the drug particles intracellular. There is several mechanisms at cellular level that contribute to drug resistance, and the internalization rate and mechanism can vary depending on the characteristics like size, coating and charge of the NPs.

## 2.5 Different in-vitro and in-vivo tumor models

Due to the heterogeneity of cancer it is a difficult disease to cure, and researchers are working hard to improve both the understanding of the disease as well as the treatment options.

An overall goal when conducting cancer research is to perform the experiments in environments as close to the human body as possible. As the mouse genome is very similar to the human one, in-vivo mouse models make it possible to simulate a diverse range of biological characteristics of the development, growth, and metastasis of human tumor cells [31]. On the contrary, in-vitro studies are still not sufficiently replicating these characteristics, limiting the value of in-vitro data. Graudejus et al. list four advantages [32] of in-vitro research over in-vivo as

1. Tight control of the chemical and physical environment
2. reduced cost
3. higher throughput
4. Reduced animal use

With this in mind, finding a method to conduct in-vitro studies that produce comparable results as in-vivo is of high interest.

### 2.5.1 2D vs 3D in-vitro models

Laboratory work using cell culture systems have been an important factor in reducing animal use in research, while still providing important insight and discoveries ultimately contributing to the evolution of medicine.

The traditional in-vitro cell culturing system is the 2D culturing of cells in monolayer. This method was long used in cancer research and for other biomedical purposes, but has some limitations. The 2D cultures lack the ability to mimic the natural environment and characteristics, such as the structure and physiology, of in-vivo tumors. The absence of ECM and cell-matrix interactions is a crucial factor of why these cultures fall short, as the reciprocal communication between cells and the ECM controls important factors like proliferation and cell-growth.

When comparing 3D models to their 2D counterparts, several differences become apparent. Firstly, the presence of ECM and these cell-matrix interactions allows for a more comprehensive understanding of cellular behaviour. This is one of the factors highlighted by O. Habanjar et. al (2021) as advantageous aspects in 3D models over 2D models [33]. Further they go on to describe other notable distinctions. The morphology of the cells themselves are different, where the cells typically are flat and stretched in 2D cultures while they in 3D maintain their natural cellular structure. Another difference lies in the exposure of cells to the surrounding media. In 2D cultures there is a homogeneous exposure of all cells to the media, while in 3D cultures there is a heterogeneous exposure where the upper layer is more exposed than the lower ones. Differentiation potential also varies between the two culture methods. In 2D cultures cell tend to display moderate to poor differentiation, while cells in 3D models demonstrate enhanced

differentiation. Lastly, when it comes to drug- and treatment sensitivity, cells in 3D structures have demonstrated reduced sensitivity compared to the ones in monolayers.

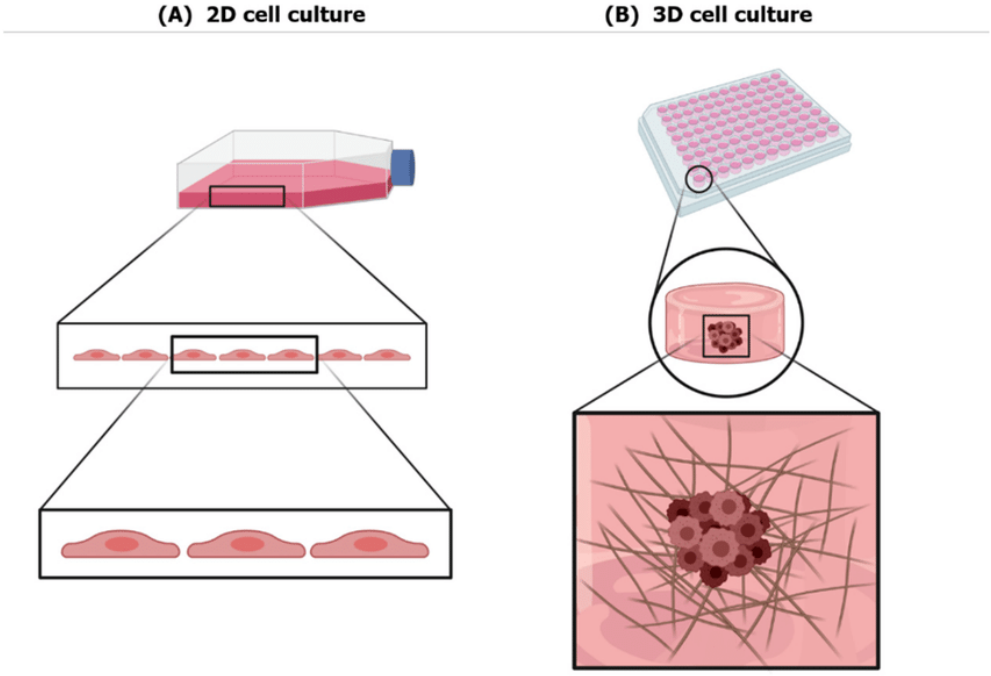


**Figure 2.6:** Illustration showing the differences between cell-cell/cell-matrix interactions in 2D vs 3D in-vitro cell cultures. The 3D cell culture shows increased cell-cell contact, as well as the presence of ECM components giving rise to cell-matrix interaction [34].

## 2.6 Spheroids as a tumor model

L.B. Weiswald et.al (2015) classify all spherical tumor models in four different groups: 1) multicellular tumor spheroids, generated in nonadherent conditions from single-cell suspensions; 2) tumorospheres, models of cancer stem cell cultures and expansion; 3) tissue-derived tumor spheres, formed only by cancer cells after partial dissociatetion of cancer tissues and 4) organotypic multicellular spheroids, generated by cutting cancer tissue under nonadherent conditions.

This thesis concerns multicellular tumor spheroids, here called multicellular spheroids or MCSs. The term MCSs will be used when referring to spheroids of two or more different cell types, in contrast to monospheroids/homospheroids which consists of only TCs. The three other groups of spherical tumor models will therefor not be explained any further, and when addressing 3D models or using the term "spheroids" it will be referencing MCSs.

The use of MCSs first pioneered in the 1970s [35][36], and since then there has been established various different methods for MCS production. These methods are commonly classified as scaffold-based and scaffold-free techniques. In scaffold-based tech-

niques, the cells are grown in the presence of either hydrogel-based or polymeric hard material-based support [37] [38]. For non-scaffold-based methods, the cells are allowed to self-aggregate to form MCSs. Some of these teqniques are more advanced than others, but the spheroids produced are usually consistent in shape and size, and mimic solid tissues by secreting their own ECM. Two examples of non-scaffold based methods are the liquid overlay method (Figure 2.7a) and the nonadhesive hydrogel micro-mold method (Figure 2.7b) [39]. In the liquid overlay method, a cell suspension is seeded into flat tissue culture flasks coated in a low-adhesive surface like agarose [40], allowing the cells to self-aggregate and form MCSs. While this technique is easy, it often leads to MCSs heterogeneous in size and shape. The micro-molded nonadhesive hydrogels method again uses hydrogels like agarose to cast micro-molds. The cells are seeded into the molds where they settle to the bottom and form spheroids due to absence of attachment to the hydrogel. This method can be used to form MCSs of different shapes, and allows for the production of MCSs in a more controlled environment [41].

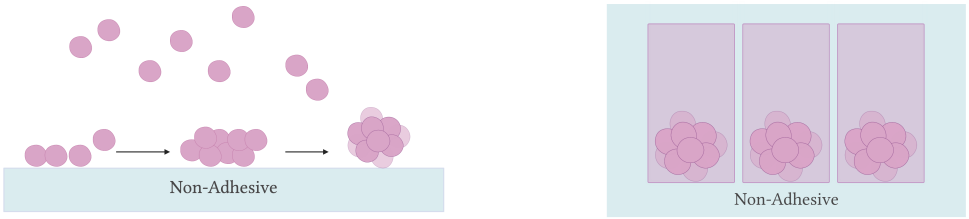


**(a)** Liquid overlay **(b)** Nonadhesive hydrogel micro-molds

**Figure 2.7:** Illustrating two methods for spheroid production a) the liquid overlay method and b) the nonadhesive hydrogel micro-mold method. Figure inspired by [39] and created in Biorender.com

### 2.6.1 Formation of spheroids

It has previously been reported that the first of three critical steps in MCS formation is the aggregation of dispersed cells [38][42][43]. Some ECM fibers, that contain cell adhesion motifs, bind tightly to integrins on the cell membrane surface, drawing the cells closer together. This ultimately leads to direct cell-cell contact, which results in the next step; up-regulated cadherin expression, and then cadherin accumulation at the membrane surface. Lastly, homophilic cadherin-cadherin bindings strengthen the cell-cell contacts leading to MCS formation and spheroid compaction. A summery of this three-step process, can be seen in Figure 2.8. The ECM fibers, integrins, and type and concentration of cadherin may vary between cell lines, but the overall process remains. In addition, adhesive proteins contributes to formation by influencing cell-cell contact, and the cytoskeleton undergoes changes that provides structural stability [38].

A requirement for cells to form multicellular spheroids is that the cells produce extracellular matrix constituents. Spheroids of only epithelial cells will produce some ECM, but will have a lower concentration than what is found in tumors in-vivo. Adding ECM producing fibroblasts, and creating heterogeneous MCS, is a therefore a common procedure.

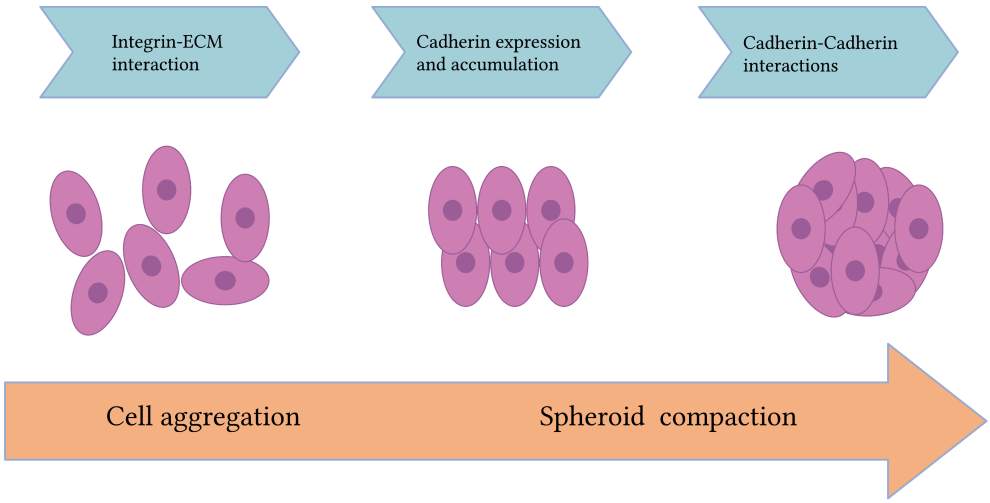


**Figure 2.8:** Step-by-step process of multicellular spheroid (MCS) formation. Cells are loosely bonded via integrin-ECM interactions. Next, a delay stage where cadherin is up-regulated and accumulated on the extracellular surface. Lastly, the formation of a compact MCS due to homophilic cadherin-cadherin interactions. Figure inspired from [38] and created in Biorender.com.

## 2.7 Confocal laser scanning microscopy

### 2.7.1 Fluorescense

Fluorochromes are molecules that can absorb energy from photons, and then re-emit this energy as fluorescence. The energy of the incoming light must match the energy gap between states in the molecule. The outgoing photon is of energy lower than the incoming one, and the difference between energy in the absorbed and emitted photon, the stokes shift, needs to be sufficiently large to be able to differentiate between the two.

Fluorescence microscopy is a microscopic technique that takes advantage of the absorbing and emitting properties of fluorochromes. To be able to image with this microscopy technique, the molecules or cells of interest must be labeled with a fluorochrome. Some limitations of conventional epifluorescent microscopes include narrow depth of field. When imaging an object thicker than the axial resolution, the picture will have reduced contrast. All parts of the sample are evenly illuminated by the light source, and

the resulting fluorescence is detected together with an out-of-focus background.

### 2.7.2 Confocal Laser Scanning Microscopy (CLSM)

In contrast to conventional epifluorescent microscopy, confocal microscopy rejects out-of-focus light enabling high-resolution imaging in thicker samples. Modern confocal microscopes include basic components like pinholes, objective lenses, and low-noise detectors in combination with lasers, mirrors, and filters for wavelength selection. The illumination- and detection-side pinholes are placed in the same conjugate plane, hence the name of the method. There are several techniques for constructing the confocal image. In the original set-up, the scanning of a moving microscope stage with fixed optics was used, however in modern times scanning of the illumination beam across a stationary sample is more common.

In CLSM, where illumination and detection are confined to a single point, the laser beam is scanned across the sample across the x- and y-direction of the field of view using mirrors, before repeating the process for each layer of the optical section. A 3-dimensional reconstruction of the sample can be produced by collecting a z-stack by changing the focal point and repeating the scanning process of all sections. The full set-up can be seen in Figure 2.9.

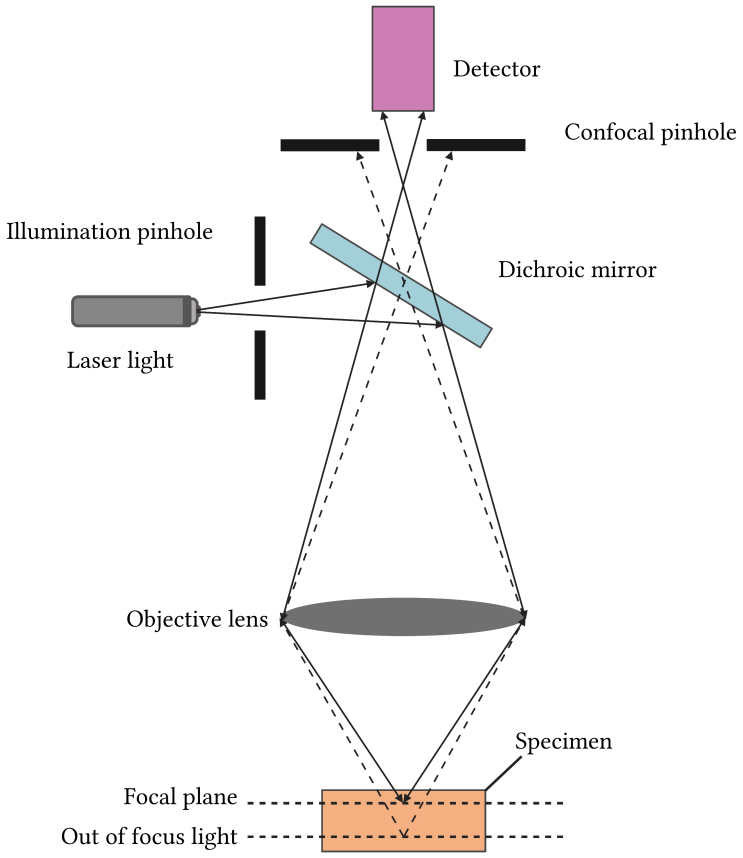


**Figure 2.9:** Schematic illustration of the principle of confocal laser scanning microscopy. Inspired by [44]and [45], created with Biorender.com

## 2.8 Colorimetry

Colorimetry is the measurment of colors and is a technique used to determine the concentration of a coloured compound in a solution [46]. When light passes through a solution, a part of the light radiation is absorbed. A colorimeter measures the intensity of the incident and transmitted light at a specific wavelenght, and from this the absorped light can be calculated. Absorption also calculates

The concentration can then be determined from the Beer-Lambert law, where absorption is in a linear relationship with concentration (2.1). Beer-Lamberts law is given by

$$A = log(\frac{I_0}{I}) = \epsilon lc \tag{2.1}$$

Where $A$ is absorbance, $I_0$ is the intensity of the incident light, $I$ the intensity of transmitted light, $\epsilon$ the molar absorptivity (in $\mathrm{mol\,L^{-1}\,cm^{-1}}$), $l$ the path length through the cuvette (in cm) and $c$ the concentration (in $\mathrm{mol\,L^{-1}}$).

There are some criteria for Beer-Lambert law to hold. Firstly the light needs to be monochromatic, and the soution needs to be homogenous. To avoid any distrurbances of the readings it is also important there is no molecules present in the that exhibits fluorescence upon excitation. Lastly, constant temperature of the solution is crutial as the molar absorptivity depends on it.

# Chapter 3

# Methods and Materials

## 3.1 Cell Culture

Cell lines 4T1 [ATCC, CRL-2539] and CT26 [ATCC, CRL-2638] were both grown in ATCC-RPMI-1640 Medium. [ATCC, 30-2001] The medium is supplemented with fetal bovine serum (FBS) [Sigma Aldrich, F7524-500ML] until the final serum concentration of 10%. The NIH/3T3 cells were cultivated in Dulbecco's modified Eagle medium (DMEM)[ATCC, 30-2002], and supplemented with Bovine Calf Serum [ATCC, Catalogue Number 30-2030] to the final serum concentration of 10%. The KPC cell line was established at the Department of Oncology at the Massachusetts General Hospital and comes from transgenic KPC mice. The cells were cultivated in Dulbecco's Modified Eagle Medium (DMEM 1X) [Gibco, reference Number: 11960-044] supplemented with FBS and 200 mM L-glutamine [Sigma Aldrich, G7513-100ML] to final serum concentration of 10% and 0.5% respectively. All cells were seeded in T75 cell flasks [VWR, 734-2313], and incubated at 37 °C with 5% $CO_2$ concentration. During subcultivation cells were washed with PBS, and detached using trypsin/EDTA [Sigma Aldrich, T4049-500ML].

It is of relevance for further reading to have an overview of the different cell lines and their corresponding growth mediums. This information is therefore summarized in Table 3.1

**Table 3.1:** Overview of all the cell lines used and their optimal growth medium.

| Cell line | Cell type | Growth medium |
|---|---|---|
| 4T1 | Tumor cells | ATCC RPMI-1640 |
| CT26 | Tumor cells | ATCC RPMI-1640 |
| KPC | Tumor cells | Gibco DMEM 1X |
| NIH/3T3 | Fibroblasts | ATCC DMEM |

## 3.2 Subculture Procedure of Cells in Monolayer

The cells were observed using phase contrast microscopy , and subseeded before the point of confluency was reached. 4T1 and CT26 followed the same sub-cultivation routine, with re-seeding every 3-4 days, with one medium change in between. The NIH/3T3 cells also have a lower recommended maximum confluency before re-seeding, and were therefore monitored more closely and were sub-seeded on average every 3 days. KPC cells is recommended to be split every other day at a 1 : 2 ratio, and this was followed most of the time. At times the cells were left until day 3 before subseeding, and the splitting ratio was then reduced.

Cell medium, PBS, and trypsin/EDTA were heated in a water bath at 37 °C for 15 min before sub-seeding. Heated reagents together with the T75 flask with the cells, were brought into the Laminar Flow Bench (MaxiSafe 2030i [Thermo Fisher, 51032711]). The old medium was removed before the cells were washed twice with 5 mL of PBS. Next, 1 mL of trypsin was added, and the flasks were incubated for around 5 min until the cells were detached from the bottom. The trypsin was then neutralized by adding 9 mL of cell medium. Around 2 mL was transferred to a 15 mL tube, before being brought to the Countess™automated cell counter[Invitrogen ™]. The concentration of cells/mL was then determined. 10 µL of a well-suspended cell suspension was added to both sides of the Countess cell counting slides.

An appropriate amount of cell medium, depending on the cell concentration, was then transferred to a new cell flask. For 4T1 and CT26 the subseeding ration was usually kept constant at 1/10. For NIH/3T3 the number of cells seeded was around 250.000. The The KPC cells were subseeded every other day at a 1:2 ratio as recommended.

### 3.2.1 Cell counting using Bürker chamber

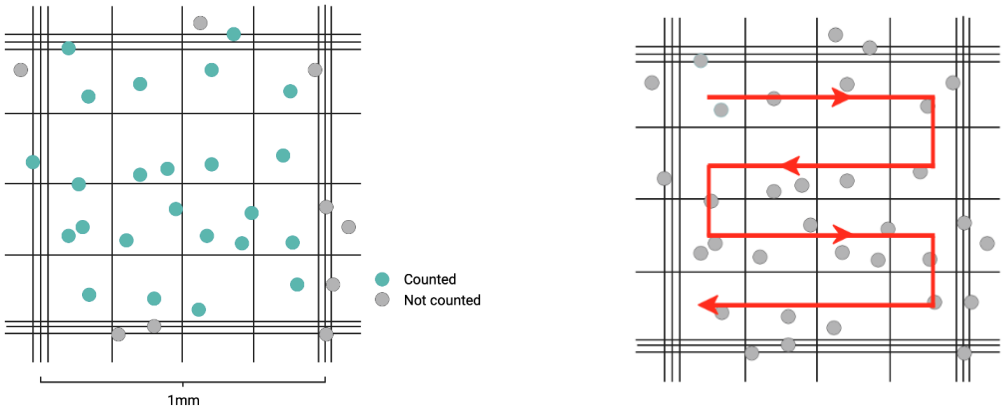


**(a)** **(b)**

**Figure 3.1:** Illustration of how to count cells in Bürker chamber. Figure a) shows which cells to include in the counting, while figure b) displays the direction of counting.

For simplicity an automatic cell counting system Countess was often used during subseeding. In steps where a more accurate number of cells needed to be seeded, or it was important to calculate accurate cell population, the Bürker chamber [Marienfeld Superior, 0640210] was used. The Bürker chamber is a special glass slide containing a grid for counting cells. The specific grid used consisted of 9 larger squares of $1\,\mathrm{mm}^2$, as seen in Figure 3.1a. A cover glass was attached to the glass slide after moistening the slide using exhaled breath. A single-use plastic pipette contaning the cell suspension was then placed on the edge, and the cells suspension was automatically drawn in beneath the cover glass through capillary forces. This was repeated for both sides of the counting chambers.

The cells were then counted in 3 of the squares, for both sides in the direction shown in Figure 3.1b. The cells on the edges, marked by triple lines, were only counted on two of the sides. Number of cells per mL were then calculated using this formula:

$$\frac{\text{Counted cells} \times 10^3}{\text{Area counted } (\mathrm{mm}^2) \times 0.1\,\mathrm{mm}} = \text{Cells per mL suspension} \tag{3.1}$$

## 3.3 Production of Multicellular Spheroids

For the production of MCSs, bot the micro-molded nonadhesive hydrogel method and the liquid overlay method was used. For the nonadhesive hydrogels, agarose (Agarose Type I-A, low EEO [Sigma Aldrich, A0169]) and agar-agar [Sigma Aldrich, A1296] was used respectively. The MCSs were initiated from cells in monolayer cultures, and all consisted of the fibroblasts NIH/3T3 in combination with a tumor cell line (4T1/CT26/KPC). The TC-to-fibroblast ratio was determined to be 1:5, as a previous study of 4T1/3T3 spheroids stated this ratio provided the MCSs with similar characteristics as clinical breast tumor [47].

### 3.3.1 Agarose Micro-Mold Method

#### Preparation of 1.5% agarose solution

A 1.5% agarose solution was prepared by weighing 2.25 g agarose powder, and adding it to a 250 mL lidded glass bottle with 150 mL Elix-$H_2O$. The lid was then screwed on loosely, before the solution was sterilized in an autoclave at 120 °C for 15 min. The agarose powder dissolved and becomes liquid at 90 °C, and later forms a hydrogel at temperatures below 40 °C this. Optimal working temperature was around 70 °C, as it quickly cools down and solidifies. The agar solution was either used warm, directly from the autoclaved, or it was heated using a magnetic stirrer.

### Making the 3D Petri Dish®

The 3D Petri Dish®(Microtissues®) is a natural 3D cell environment suitable for growing spheroids. It provides an environment that maximizes cell-cell contact which drives self assembly of spheroids without additional scaffold. The 3D Petri Dish® is a #24-96 (array 8x12), which means it contains 96 wells inside one dish, which fit inside a standard 24-well tissue culture pack. The wells of the finished 3D Petri Dish® have a diameter of 400 µm and depth of 800 µm.

All equipment and materials used during the process was sterilized, and the work was perfomed in a sterile bench. The 3D Petri Dish® is made by pipetting 330 µm of agarose into a silicone mold. After the agarose cools down and solidifies, the 3D Petri Dish® can be carefully removed from the mold using a spatula. The silicone mold, the mold with the agarose, and the finished agarose 3D Petri Dish® can be seen in Figure 3.2. The lack of cell adhesion motifs present in agarose cause cells suspended in the agarose molds to not attach to the surface but instead form spheroids.

**Figure 3.2:** Images from different stages of preparation of a 3D Petri Dish®. From the left: Silicon mold, silicon mold with agarose solution in, finished 3D Petri Dish® made of agarose.

The finished 3D Petri Dish® was placed in the 24-well plate with the wells facing up and washed with 1 mL PBS. The 24-well plate with the molds was then centrifuged for 5 min at 1200 rpm to remove any air bubbles trapped in the wells. The PBS was then removed and replaced with fresh cell medium and left to incubate for 15 minutes to equilibrate.

### Seeding of cells into the 3D Petri Dish®

Before seeding the cells were trypsinized, counted, and prepared using the same procedure as in Section 3.2. The volume of each well is 75 µL,and to reach spheroids with

diameters of around 200 µm a cell concentration of 96,000 cells/75 µL was recommended by the supplier. Thus, after counting, both TC and fibroblasts solutions with a concentration of $1.3 \times 10^6$ cells/mL was created. To obtain a solution with 1:5 ratio, appropriate volumes of the TC- and fibroblast-solutions were combined into a new tube. Most times the volumes were 83 µL and 417 µL respectively. Occasionally, the total amount of cells at the day of the experiment was too low, and volumes were scaled down accordingly while making sure the total volume was large enough to seed all the 3D Petri Dish® needed.

From this combined solution 75 µL was extracted, and carefully seeded drop wise into the cell seeding chamber of the agarose mold. It was then left for 10 min to settle into the wells before an additional 1 mL of cell medium was added into each mold. The lid was then placed back on the 24-well plate and placed into the incubator. If left over a longer period, the cell medium was changed on day three.

### 3.3.2 Liquid overlay method using Agar

A 1% agar solution was prepared as first weighing 1 g agar and added to 100 mL Elix-$H_2O$ in a 250 mL lidded glass bottle. The lid was loosely screwed on, and the solution was sterilized in an autoclave at 120 °C for 15 min. As for the agarose powder, agar is dissolved and becomes liquid at around 90 °C, and forms a hydrogel for temperatures below 40 °C.

To prepare the agar flasks, 9 mL of the liquid agar solution was transferred into TC75 flasks, ensuring even distribution across the entire flask surface. The lids were loosely placed on the flasks, which were left to cool down. Subsequently, the flasks were wrapped in aluminium foil and stored at in a refrigerator. On the day of seeding, the 1% agar flasks were allowed to reach room temperature and then seeded with a total of approximately 2 million cells, comprising 330,000 TCs and 1,670,000 fibroblasts, to obtain the TC-to-fibroblast ratio of 1:5.

## 3.4 Growth characterisation of cells and spheroids

### 3.4.1 Estimation of doubling time for the various cell lines

Six T25 flasks [VWR, 734-2311], for each cell line, was seeded with $0,1x10^6$ cells. To track the growth, the total cells at each day were counted using a Bürker chamber on subsequent days.

The log phase was determined by visual evaluation, and linear regression was performed on the data on a logarithmic y-axis, obtaining an equation in the form $Y = kt + lnY0$, where $k$ is the rate constant and $lnY0$ is the starting population in the same logarithmic

units as $Y$. Doubling time is calculated as

$$DT = ln(2)/k. \tag{3.2}$$

As the functions were adjusted for two separate variables, the 95% confidence intervals (95%CI) given, was very high. To decrease the uncertainty, $lnY0$ was set constant equal to the extrapolated intersects at the y-axis, and the functions were readjusted with $k$ as the only free parameter.

### 3.4.2 Growth Curve of copheroids

To measure the time it took for the spheroids to double in volume, the volume-DT (V-DT), were measured. For this experiments, four agarose molds with 96 spheroids were prepared for each of the tumor cell lines. To investigate if the choice of medium effects the growth, half of these were cultivated in the corresponding T-GM, and the other half in the F-GM.

The growth was monitured over 5 days, and the MCSs were imaged using phase contrast microscopy with a camera attached. The camera was Nikon Eclipse TS100-F laboratory microscope with Nikon's Digital Sight DS-Fi1 (5M2) camera head, and Nikon Digital Sight DS-L2 imaging controller. The most used objective was CFI Plan Fluor 10X W [Nikon, MRH07120], but the equivalent lenses in 5X and 20X were also used. The NIS-Elements BR software was used both to capture the images

The MCSs were later manually measured using software Fiji-ImageJ. A total of 40 spheroids were analyzed for each cell line, with 20 spheroids randomly chosen from each parallel set of the same type of spheroid. Two perpendicular diameters ($a$ and $b$) was measured, and the volumes were calculated with the assumption that the third diameter is equal to the shortest of the two measured diameters. This yields the equation for the volume, $V$ as

$$V = \frac{\pi}{6} ab^2. \tag{3.3}$$

Figure 3.3 illustrated how the diameters were measured in ImageJ. Wells containing multiple spheroids, as in Figure 3.3 (b), were excluded from the analysis. It is also important to note that the images were not automatically calibrated. However to establish an accurate scale, a manual calibration process was conducted using the known width of the wells, which measures 400 µm. Further, the V-DT for the MCSs was calculated in the same manner as the DT in monolayer.

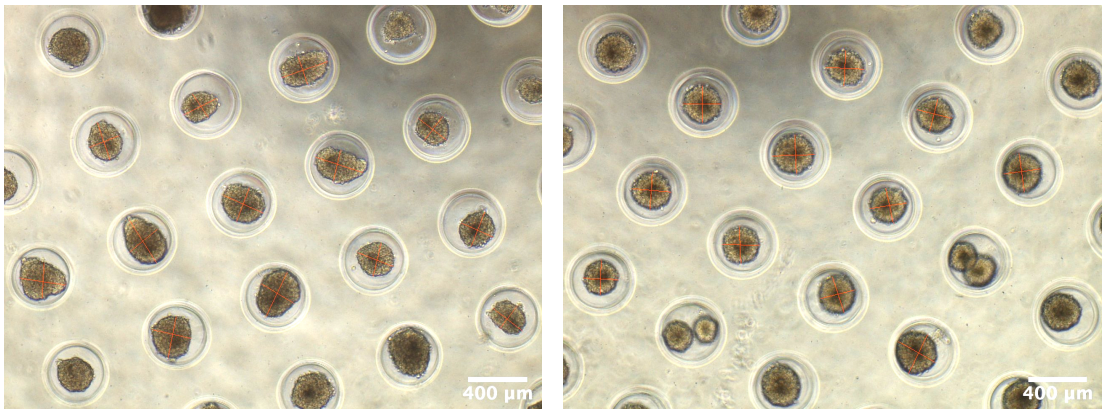


**Figure 3.3:** Example images illustrating how the diameter measurements was done on spheroids in ImageJ.

## 3.5 Distribution of fibroblast and tumor cells

In the specialization profect, the distribution of fibroblasts and TCs within the MCSs were examined for CT26 and 4T1. To be able to view the organization between the different cell types within the MCSs, the cytosol were labeled in different colors and then imaged by CLSM. Some differences were observed, but the experiment was repeated to confirm the observations, as well as getting information on the distribution within KPC MCSs. The optimal dye concentration was tested in the specialization project and determined to be 5 µM, in agreement with the protocol from the supplier. The samples were also previously checked for any background fluorescent and overlaps in the emission spectra.

The labeling was done using Invitrogen CellTrace™Proliferation Kit in Violet [Thermofisher, C34557] and CFSE [Thermofisher, C34554] (see Table 3.2). The dye does not bind to the lipid membrane, but easily crosses the plasma membrane and binds inside the cell [48]. It provides a stable signal even after several days in a cell culture environment, up to 5 cell generations. The kit contains 1 single-use vial of dry dye and a stock solution of 5 mM is created by dissolving the contents in anhydrous DMSO before use.

**Table 3.2:** Exitation/emission maxima, and recommended excitation source during fluorescent imaging, for two different fluorescent dyes.

| CellTrace™reagent | Ex/Em maxima | Recommended excitation source |
|---|---|---|
| CellTrace™Violet | 405/ 450 nm | 405 nm |
| CellTrace™CFSE | 492/ 517 nm | 488 nm |

### 3.5.1 Fluorescent labelling of spheroids

The MCSs were grown using the same procedure previously described in Section 3.3.1, with an additional step of labelling the cells before seeding into the 3D Petri Dish®. Six 3D Petri Dish® was made in total, two for each spheroid model.

The method described was performed in parallel for each cell line. After trypsinizing and counting the cells, a volume corresponding to 1 million cells were transfered to a 15 mL tube. The cells were pelleted by centrifugation (1500 RPM for 5 min), and the supernatant was removed before the cells were gently resuspended in 1 mL of PBS. Next, 1 µL of stock solution of dye was added to the cell suspension to obtain the final working solution of 5 µM. Cells were then incubated at 37 °C for 20 min protected from light. 5 mL of cell medium was then added to the tube before it was incubated for additional 5 min. Cells were centrifuged again, and resuspended in 770 µL fresh culture medium, obtaining a final cell concentration of 1.3 million cells/mL for both the TC and fibroblasts solutions. Appropriate volumes of the desired TC solution and fibroblasts solution was then combined to obtain the 1:5 ratio. Subsequently, 75 µL of the combined solution was seeded into the 3D Petri Dish® as previously described.

### 3.5.2 Preparation of samples for Confocal Laser Scanning Microscopy

The spheroids were imaged on day 2 after seeding. On the day of imaging, the spheroids needed to be removed from the microwells. This was done by carefully removing the GM before removing the 3D Petri Dish® from the 24-well plate, and placing it upside down in a new one. 1 mL of cell medium was added into the wells before the plate was centrifuged for 5 min at 500 rpm. Further, the empty 3D Petri Dish® was removed, and the solutions now containing the MCSs were transferred into 15 mL tubes. The tubes were then centrifuged for 2 min again at 500 rpm before the supernatant was removed, and replaced with 1 mL of PBS. Lastly, 300 µL of this final solution was extracted and placed into an Ibidi $\mu$-slide 8 well [Ibidi, 80826]. The samples were now ready to be imaged with CLSM.

### 3.5.3 Imaging of MCSs using CLSM

CLSM was performed using LSM 800 Airyscan Confocal Microscope (Carl Zeiss AG, Germany) using lasers with the recommended wavelengths 405 nm and 488 nm as seen in Table 3.2 and objective C-Apochromat $40X/1.20$W Corr M27 (Carl Zeiss AG, Germany) Imaging was done using bi-directional sequential scanning. Laser intensity, gain and imaging settings varied from time to time, but were tuned to utilize the whole grey scale using the software Zeiss Zen (blue edition). Acquisition settings is summarized in Table 3.3.

In a few of the samples there were some very bright areas, making it difficult to keep

all information without damaging the detector.

**Table 3.3:** Acquisition settings for CLSM imaging for colocalization of tumor cells and fibroblasts to view cellular distribution of spheroids.

| **Fluorophore** | **CellTrace Violet** | **CellTrace CFSE** |
|---|---|---|
| **Laser Wavelength** | 405 nm | 488 nm |
| **Excitation Wavelength** | 353 nm | 493 nm |
| **Emission Spectrum** | 410-470 nm | 510-600 |
| **Pinhole Diameter** | 1 AU | 1 AU |
| **Laser Intensity** | 5 % | 5 % |
| **Detector Gain** | 524 V | 524 V |
| **Detector Offset** | 0 | 0 |

The signal from the core started being weaker at around 60 µm into the MCSs, and images were taken with a depth at, $\Delta z = 50\,\mu m$ from the bottom of the MCSs.

## 3.6 Determining contents of collagen and sGAG in different MCSs

Collagen and sGAG assays was performed for MCSs with the fibroblasts and 4T1, CT26 and KPC as in the previous experiments.

This method was previously tested and optimized for harvested in-vivo tumors from mice after implantation of the same cancer cells (4T1, CT26, and KPC). This was done by Håkon Fossland Wesche in his specialization project [49]. The following protocol (expect for sample preparation) is therefore adapted from his project, in combination with the protocol given from the suppliers of the assays.

### 3.6.1 Sample preparation

MCSs were cultivated in agar flasks following the procedure described in Section 3.3.2. The flasks designated to sGAG measurements was seeded with a total of 2 million cells in a 1:5 ration, as per standard protocol. As a test run had revealed collagen levels below the detection limit, flasks for collagen were seeded with 4 million cells, still with ratio 1:5. A total of 12 flasks were prepared, with half allocated for the sGAG assay and the other half for the collagen assay. Two parallels were created for each cell line within each assay. However, due to limited reagent availability, only one of the flasks were used for sGAG measurements.

After incubating for 2 days, the contents of the flasks were transferred to 15 mL tubes and centrifuged at 1500 rcf for 5 minutes. The majority of the supernatant was care-

fully removed, leaving approximately 1 mL of the medium in the tube. The remaining medium and pellet were transferred to pre-labeled, pre-weighed 1.5 mL microcentrifuge tubes. These tubes were subsequently microcentrifuged at 3000 rcf to ensure a tightly-packed pellet.

Following the second round of centrifugation excess medium was removed by gently inverting and draining the tubes, followed by tapping them on a paper towel to remove any residual liquid. Any remaining medium on the tube walls and lid was carefully removed using a cotton swab. The tubes were then re-weighed, and the weight of the pellet was determined by subtracting the initial weight of the empty tube.

### 3.6.2 Assay preparation

Half of the tubes from the previous section was used with the Sircol - Soluble Collagen Assay kit [50] , and the other half was used with the Blyscan - sulfated Glycosaminoglycan (sGAG) assay kit [51]. In the following sections the collagen and sGAG assays will be described in different subsections.

#### Enzymatic extraction and concentration of collagen

The digestion buffer was prepared with pepsin [Sigma Aldrich, P7012] at a concentration of 0.1 mg $mL^{-1}$ in 0.5 M acetic acid. The digestion buffer was added to the sample tubes at a solution-to-sample ratio of 1:20. For instance 10 mg of sample requires 200 mL of digestion buffer. The samples were incubated overnight at 4 °C on a mechanical shaker operating at 500 rpm. The following day, the samples were centrifuged at 3000 rcf for 10 minutes to re-pellet all the MCSs. To prevent enzyme self-degradation, the buffer was used on the same day it was prepared.

A preliminary assay run was conducted to assess collagen contents, which was found to be significantly low. Therefore, an additional step of collagen isolation and concentration was implemented. Acid Neutralizing Reagent [Biocolor, BB816] was added to each sample at a ratio of 1 : 10 (sample-to-solution), followed by the addition of cold Isolation & Concentration Reagent [Biocolor, BB827] at a ratio of 1 : 5 (sample-to-solution). For example, a sample of 400 µL collagen extract required 40 µL Acid Neutralizing Reagent and 80 µL Isolation & Concentration Reagent. The tubes were vortexed ($3 \times 5$ seconds), and then incubated in a pre-cooled water bath at 4 °C for 15 minutes. After incubation, further vortexing ($3 \times 5$ seconds) was performed. Subsequently, the samples were centrifuged at 13 000 rcf for 10 minutes to pellet the collagen extracts, and the supernatant was decanted as described in the sample preparation section. To wash the collagen precipitate, 1000 µL of cold (4 °C) diluted Acid-Salt Wash Reagent was added to each tube, and the tubes were carefully inverted 3 times to ensure thorough rinsing. Another round of the centrifugation (13 000 rcf) and decanting was carried out. At this stage, the sample tubes were ready for the subsequent steps of the protocol.

Next, the blanks and standards were prepared. A set of 1.5 mL microcentrifuge tubes was labeled, creating duplicates of each concentration. The Sircol protocol suggested one lower and one higher Collagen Reference Standard [Biocolor, BB708](0 − 15 µg or 0 − 50 µg) depending on the collagen levels in the samples. For this particular experiment, the lower standard curve was employed. Accordingly, collagen standards were prepared by using the 0.5 µg µL$^{-1}$ stock solution from the Sircol collagen kit to create standard solutions of 1, 5, and 10 µg concentrations. As for the reagent blanks, they received 100 µL of digestion buffer.

#### Enzymatic extraction of sGAG

The digestion buffer was prepared by combining 400 mg of sodium acetate, 200 mg of EDTA disodium salt [Amresco, 0533C338], 40 mg of cystein HCl [Sigma Aldrich, 107H0028], and 200 µL of papain [Sigma Aldrich, P3125, 100MG] suspension in 50 mL of 0.2 M sodium phosphate buffer at pH 6.4. Next, 1 mL of the papain digestion buffer was added to each sample, followed by overnight incubation in a thermally regulated heating block at 65 °C. After digestion, the tubes were centrifuged at 10 000 rcf for 10 minute. To prevent enzyme self-degradation, the digestion buffer was used within one week after the addition of the enzyme.

A set of 1.5 mL microcentrifuge tubes was labeled for samples, standards, and blanks. For the samples, 100 µL of the supernatant was transferred to a new tube. The sGAG standards were prepared using the 0.1 µg µL$^{-1}$ sGAG Reference standard [Biocolor, BB723] stock solution from the sGAG kit to create standards solutions of 1, 3, and 7 µg concentrations in digestion buffer. Reagent blanks received 100 µL of digestion buffer.

### 3.6.3 Assay

#### Collagen

To prepare the samples, standards, and blank tubes, 1 mL of Sircol Dye Reagent [Biocolor, BB721] was added to each tube. The tubes were gently inverted to ensure thorough mixing of the dye with the samples. Subsequently, the tubes were placed on a mechanical shaker at 300 rpm for 30 minutes to facilitate the formation and precipitation of the collagen-dye complex. Afterwards, the tubes were centrifuged at 13 000 rcf for 10 minutes to pellet the collagen-dye complexes. Longer centrifugation times were occasially used to ensure firm packing of the complexes. The solution containing the unbound dye was then carefully drained from the tubes.

To ensure complete removal of any residual unbound dye, 750 µL of ice-cold Acid Salt Wash Reagent [Biocolor, BB727] was gently added to each tube. The tubes were centrifuged again at 13 000 rcf for 10 minutes to wash the pellet and remove any remaining dye. The tubes were again drained, this time very precise, with tapping against a paper

sheet and excess fluid removal using cotton buds. This was the most critical draining step of the protocol, where only the dye-complex pellet was left in the tube.

To release the dye from the collagen, 250 µL of Alkali Reagent [Biocolor, BB720] was added to each tube, as recommended when using the lower collagen reference standards. The tubes were vortexed for a few seconds with 5 minutes seperation, until all dye was released into the solution. Finally, 200 µL of each sample, standard, and blank was transferred to individual wells of a 96−well Costar Clear Microwell plate [Sigma Aldrich, CLS3506] . Measurements were taken immediately after, as the solution is light stable for only 2 hours.

#### sGAG

For each sample, standard and blank tube, 1 mL of Blyscan Dye Reagent [Biocolor, BB718] was carefully added. The tubes were then subjected to thorough mixing by inverting and subsequently placed on a mechanical shaker at 300 rpm for 30 minutes. Following the incubation period, centrifugation at 13.000 rcf for 10 minutes was performed to pellet the precipitated sGAG-dye compelxes in the samples. Careful drainage of the unbound dye solution from the tubes was then carried out. To release the bound dye into the solution, 0.5 mL of Blyscan Dissociation Reagent [Biocolor, BB730] was added to the tubes, followed by vortexing until complete dissolution of the dye was acheived. To remove foam, the tubes were centrifuged again at 13 000 rcf.

Subsequently, 200 µL of each sample, standard and blank solution was added to individual wells of a 96−well Costar Clear Microwell plate. To ensure accuracy in absorbance measurements, any bubbles present in the wells were carefully removed using a 70% ethanol mist and a small pipette tip dipped in ethanol. Again, to avoid dye bleaching, measurements were performed immediately after completion of the protocol.

### 3.6.4 Absorbance measurements

The absorbance readings were performed using the Spectramax i3x plate reader in combination with the Softmax Pro 6.5.1 software.

#### Collagen measurements

The plate reader was configured to perform endpoint absorption measurements with a wavelenght of 556 nm. The microwell plate was positioned in the plate reader, and absorbance readings of the wells were subsequently taken. Using the Softmax software, the wells were designated as unknowns, standards or blanks (referece solutions) for further analysis. The software utilized the absorbance values obtained to generate a standard curve, which correlated the absorbance readings of the unknown samples to

a concentration in mg. The concentrations adjusted for the weight of the pellet, which enabled the final concentration to be expressed as µg collagen per mg MCSs.

#### sGAG

The plate reader was set to endpoint absorption measurements using a wavelength of 656 nm. Further, the Softmax software was employed in the same manner as for the collagen assay. In contrast to the collagen samples that were concentrated, sGAG concentrations needed to be adjusted for dilutions carried out during the assay as well as the weight of the original pellet. This again ensured the final concentration was given as µg sGAG per mg MCSs.

## 3.7 Nanoparticle uptake into MCSs

Investigation of penetration of NPs into spheroids was done by incubating spheroids with NPs for 3, 6, and 24 hours before imaging with CLSM. To more accurately compare results to the distribution experiment, spheroids were harvested at 2 days after seeding. The NPs used for this experiment were FluoSpheres™carboxylate-modified microspheres of sizes 0.04 µm [Thermo Fisher, F8793] 0.1 µm [Thermo Fisher, F8801] in the color red (580/605).

### 3.7.1 Optimizing NP concentration and time period

A test run using different concentrations of the 100 nm NP was done to find the optimal concentration for the following experiments. In a similar experiment using the same NPs, a concentration of $5\,\mu g\,mL^{-1}$ was used [27]. This corresponds to $0.25\,\mu L\,mL^{-1}$ (NPs 2% solids), and was used as a starting point. The concentrations tested were $0.25\,\mu L\,mL^{-1}$, $1.25\,\mu L\,mL^{-1}$ and $2.5\,\mu L\,mL^{-1}$. For simplicity, no fluorescent labelling of cells were performed. The spheroids with NPs were placed to incubate in cell medium on a shaking table at room temperature. The centre of the spheroids were imaged using CLSM after 3 hours and 24 hours. The imaging setting, laser intensity and gain were fine tuned for the highest concentration to avoid saturation and these settings were then used for imaging of samples of all concentrations.

The lowest concentration, $0.25\,\mu L\,mL^{-1}$ was determined to be high enough, and the following NP uptake experiment only used this concentration. Very few NP had penetrated into the MCSs after 3 hours, and any imaging at shorter incubation times was considered uninteresting. A choice of not testing NPs larger than 0.1 µm was also done as penetration for this size NPs was also low even after 24 hours. Imaging from the trial run can be seem in the Appendix B.

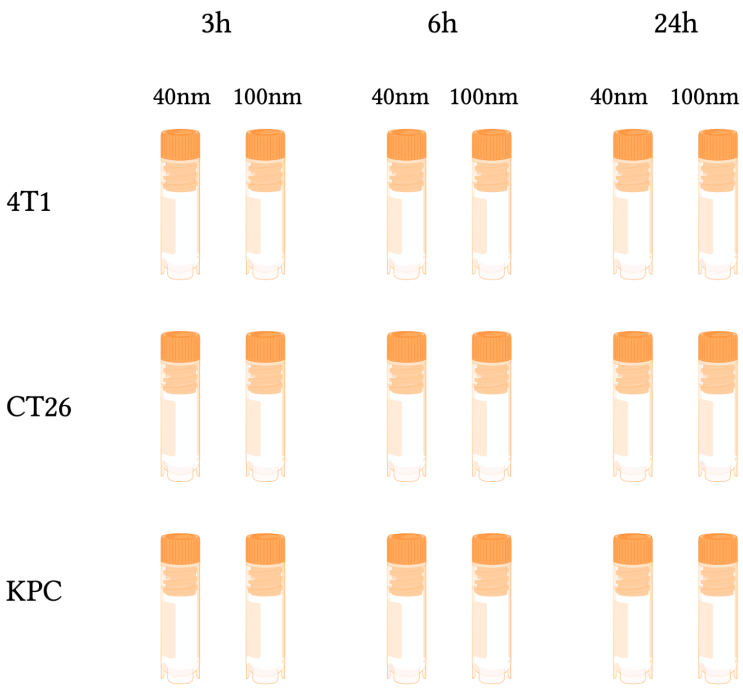


**Figure 3.4:** An illustration of the sample set-up for nanoparticle uptake measurements. This included 18 cryotubes, 6 for each of the TCs, including separate tubes for imaging at 3, 6, and 24 hours for two different sized nanoparticles. Created in Biorender.com

### 3.7.2 Measurement of size and time dependency of NPs in MCSs

For the main experiment, the NP uptake was measured in all of the three different type of MCSs using both NP sizes, 40 nm (5% solids) and 100 nm (2% solids). The concentration was kept at 5 µg mL$^{-1}$ this corresponded to 0.1 µL mL$^{-1}$ and 0.25 µL mL$^{-1}$ for the 40 nm and 100 nm respectively. The uptake was tested at three time points, after 3, 6, and 24 hours. This gave 18 separate sample tubes to be created as seen in Figure 3.4, 6 for each tumor cell line.

For this experiment the MCSs were cultivated in 3D Petri Dish® as in Section 3.3.1, and were labelled as in Section 3.5.1 where TCs were labeled with CellTrace™Violet and fibroblasts with CellTrace™CFSE. Volumes were adjusted to make sure there was enough cells to seed the desired number of agarose molds.

On day 2 after seeding, the spheroids were removed from the mold as described in Section 3.5.2, by inverting the agarose molds and centrifuging at 500 rcf for 5 minutes. 1 mL of the suitable TC-GM was added to each well, and the solution with the MCSs was transferred to a 15 mL tube. Next, after careful resuspension of the solution, 300 µL was transferred into three separate 1.5 mL tubes. Before addition of the nanoparticles were dispersed for 2 minutes using an ultrasonic bath (Branson Bransonic®CPXH Digital Bath 1800 [Emerson]. To avoid physical stress on the spheroids in the tubes, it is important to avoid any air bubbles. The 2 mL therefore needed to be filled to the

maximum capacity, and the NPs were added in the desired concentration, $0.1\,\mu L\,mL^{-1}$ (40 nm) and $0.25\,\mu L\,mL^{-1}$ (100 nm), assuming that the total volume in the full tube is 2 mL. After addition of the NPs, GM was added to the rim of the microcentrifuge tubes as well as in the lid, before placing the lid on the tube. Subsequently, the tubes were left to incubate on a mechanical rolling table in at 37 °C and 5% $CO_2$ concentration. After 3, 6, and 24 hours, the tubes were collected and left for a couple minutes until the spheroids fell to the bottom of the tube. 1.6 mL of the solution was carefully pipetted out of the tube, making sure not to remove the MCSs. Lastly, 300 µL was transferred into an Ibidi-8-well. During this step the pipette tip was kept close to the bottom where the spheroids was located to ensure they were successfully transferred into the sample.

#### CLSM imaging of uptake

For CLSM, same microscope, detector, lense and objective was used as in Section 3.5.3. The aquisition settings for all three channels is summarized in Table 3.4. The laser intensity and detector gain had to be adjusted slightly between imaging for the two NP sizes, which makes the two groups not directly comparable in terms of their intensity.

**Table 3.4:** Acquisition settings for CLSM imaging for measuring nanoparticle uptake in spheroids.

| **Fluorophore** | **CellTrace Violet** | **CellTrace CFSE** | **FluoSpheres Red** | |
|---|---|---|---|---|
| | | | **40 nm** | **100 nm** |
| **Laser Wavelength** | 405 nm | 488 nm | 561 nm | 561 nm |
| **Excitation Wavelength** | 353 nm | 493 nm | 580 nm | 580 nm |
| **Emission Spectrum** | 410-470 nm | 510-600 nm | 550-700 | 550-700 nm |
| **Pinhole Diameter** | 1 AU | 1 AU | 1 AU | 1 AU |
| **Laser Intensity** | 5% | 5% | 17% | 6.5% |
| **Detector Gain** | 524 V | 524 V | 635 | 620 |
| **Detector Offset** | 0 | 0 | 0 | 0 |

## 3.8 Data analysis

### 3.8.1 Cellular Organization analysis in ImageJ

To quantify the distribution of fibroblast in cospheroids, the two channels (TC and fibroblast) of the CLSM images were thresholded using Huang algorithm, and pixel count was performed on the CLSM images. An circular ROI was selected in ImageJ, surrounding the entire MCS. The thickness of the periphery part was calculated based on the radius of the outer circle, in such a manner that the area of the periphery and central part of the spheroid was equal. The outer circle was then shrinked correspond-

ingly using the "enlarge" selection tool, to create a smaller circle. The periphery ROI was created by using 'XOR' of the outer and inner circle. The same ROI was used for both channels, as seen in Figure 3.5.

The total pixels in both the whole region, and the periphery was calculated separately. and from those two values the percentage of pixels in the periphery was calculated. This was done both for the channel including fibroblasts and also the TC channel.

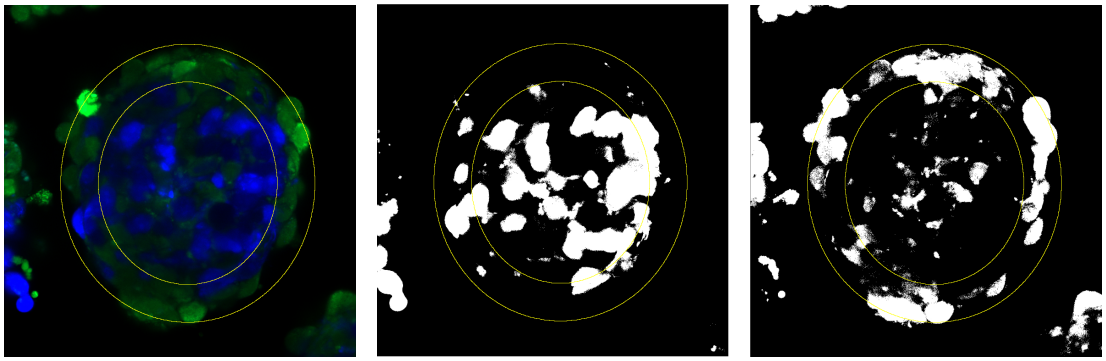

**(a)** **(b)** **(c)**

**Figure 3.5:** Region of interest (ROI) defining the periphery region in of a spheroid (imaged with confocal laser scanning microscopy) in ImageJ, a) shows the defined ROI on the composite image of both channels, b) shows the thresholded image of the tumor cells with the ROI, and c) shows the thresholded image of the fibroblasts with the same ROI.

### 3.8.2 Nanoparticle Penetration Analysis

#### Matlab Script

To assess the penetration depth of NPs within each spheroid, a Matlab script was utilized. Initially, prior to importing the CLSM images into Matlab, the images underwent thresholding using the Huang algorithm, and any NPs located outside the spheroids were cleared using ImageJ. To do this, a region of interest (ROI) at the spheroid border was defined, and any NPs outside the ROI was removed. Subsequently, the channel containing the NPs was extracted from the composite image and subjected to thresholding. The threshold value for the images was set at 65, which was determined to a good balance between noise reduction and retention of relevant information in the images.

Next, the script processed one thresholded image at a time, along with information about the pixel size of the image. The center of the spheroid was determined through a semi-manual procedure involving drawing two lines across the spheroids, one along the x-axis and another along the y-direction (Figure 3.6a) The script then calculated the spheroid center based on these lines. Within each spheroid, the script calculated the pixel intensities in concentric circles of gradually increasing radii from the center (Figure 3.6 (b-d)). The thickness of each circular region was fixed at $dr = 5\,\mu m$, and intensities was measured for circles covering an area with a final radius of $100\,\mu m$. This

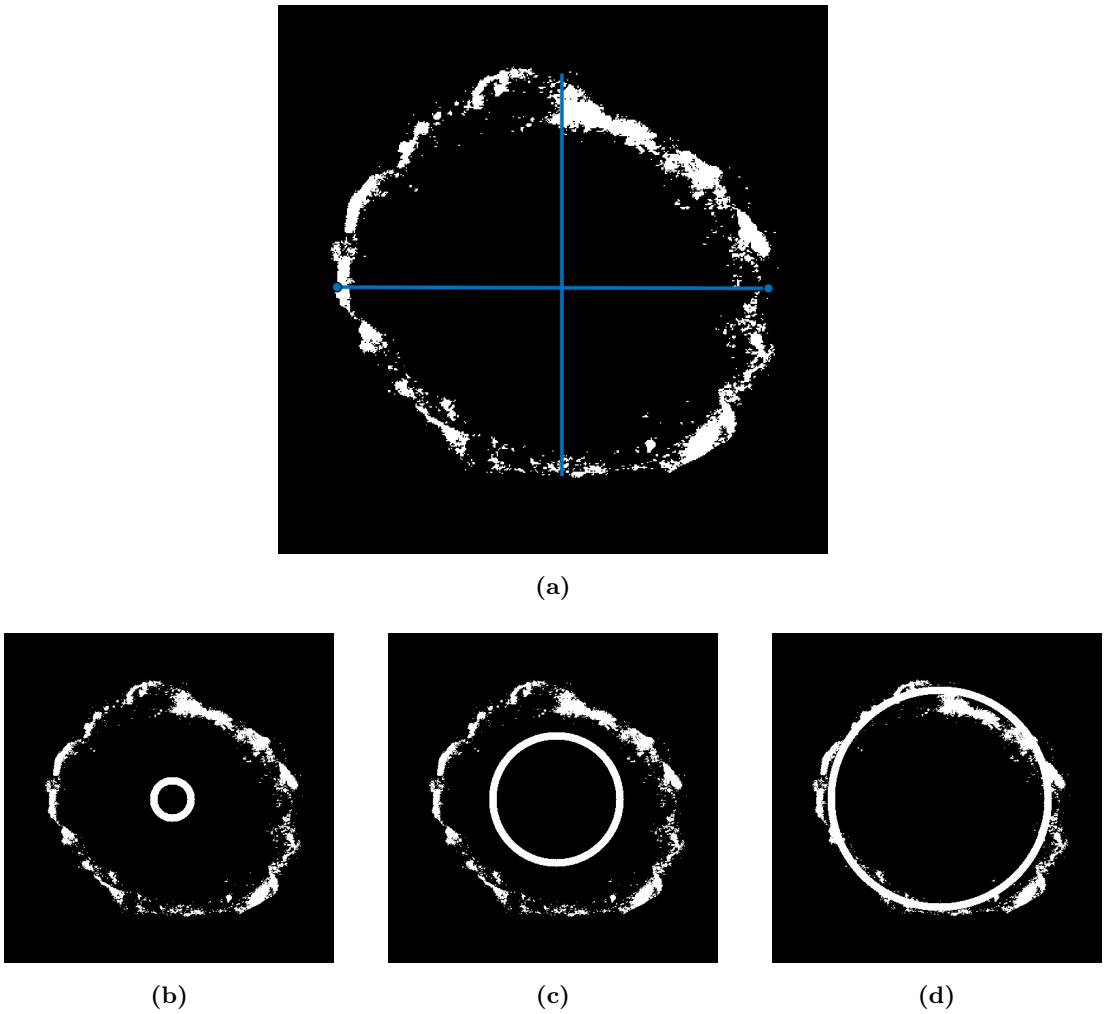

**Figure 3.6:** a) Image showing the two lines, in $x$ and $y$ direction that was manually drawn to find the center of the spheroid, b-d) Example images showing how the penetration of nanoparticles was measured utilizing a Matlab script, in which the pixel intensity within thin concentric circles propagating outwards from the center of the spheroids. a) illustrates the two lines, in $x$ and $y$ direction that was manually drawn to find the center of the spheroid

procedure generated a list of intensities, representing the amount of NPs, at varying distances from the spheroid center. The data was analysed and based on the location of the intensity peak and the radius of the spheroid, some of the data from the outermost circles was excluded. The last data point left was then set as the outer boundary of the spheroids, indicating a travelled distance of 0 µm.

### Normalization for Comparability between Data Sets

As the absolute fluorescent intensities were not comparable for different sized NPs, as different imaging settings was used. For comparability between the two groups, relative and normalized intensities was used.

The relative intensities were calculated by setting the total intensity in the MCS as 1,

and calculating the fraction of intensity at each distance. This was done for each MCS separately, before calculating the average fraction at each distance for all the MCSs in the same data set.

Additionally, the total uptake for each spheroid model over the full time line was found by taking the total intensity within each spheroid, taking the average within each experimental group, and then summing up the average total intensity for all three time points. A normalization was done for the two NP sizes separately, where the 100% was set as the average total intensity value the MCSs within each group.

## 3.9 Statistical Analysis

All the plots were made in Graphpad Prism 9.5.0 (GraphPad Software, San Diego, California USA, www.graphpad.com). Results are given as mean ± standard deviation (SD) if not else stated. Statistical analyses was conducted using Prism. To determine if differences between group were of statistical significance, a one-way ANOVA test (Tukey's multiple comparisons test) with a significance level of $p < 0.05$ was performed. This test requires normal distribution, and equality of variance between the compared data sets.

Preliminary, Shapiro-Wilk test was done to check for Gaussian distribition, and Brown-Forsythe test to check the variance. In the cases where different was found, Dunnett's T3 multiple comparisons test was performed instead Tukey's test.

Statistical significant is defined as p-value below 0.05, and are indicated with asterisks (*). Significance levels of the different number of asterisks is summarized in Table 3.5.

Correlation tests was also performed using a $\alpha$-value of 0.5. Significance levels of the correlation, $p$-value were obtained, and the correlation was significant for $p \leq 0.05$. Pearson's correlation coefficient, $r$, was calulated. The significance of the different $r$values is summarized in Table 3.6.

**Table 3.5:** Summary of how Graphpad plots the statistical significance using asterisks.

| Symbol | Meaning |
|---|---|
| not significant | P >0.05 |
| * | P <0.05 |
| ** | P <0.01 |
| *** | P <0.001 |
| **** | P <0.0001 |

**Table 3.6:** Summary of how the significance of different values of Pearssons correlation coefficient, $r$, is defined.

| r-values | significance |
|---|---|
| Negligible | 0 <r <0.1 |
| Weak | 0.1 <r <0.3 |
| Medium | 0.3 <r <0.5 |
| Strong | 0.5 <r <1 |

# Chapter 4

# Results

## 4.1 Growth of Cells in Monolayer

In-vitro morphologic characteristics of the tumor cell lines, 4T1, CT26 and KPC, as well as NIH/3T3 fibroblasts, were assessed using phase contrast microscopy. Figure 4.1 illustrates their distinct morphologies when cultivated as in-vitro monolayers, highlighting variations in cell-cell contact. The 4T1 and KPC cell lines exhibited cluster growth patterns with substantial cell-cell contact, whereas CT26 displayed minimal cell-cell contact, with individual cells growing relatively independently. On the other hand, NIH/3T3 exhibited the typical elongated and stretched out fibroblastic morphology, which lead to reduced cell-cell contact as these cells primarily connected to neighboring cells. Furthermore, a stronger association between cells was observed during the cultivation process for the 4T1 and KPC cell cultures, as these cells displayed a strong tendency to cluster tightly and and were difficult to separate. Separation required rigorous resuspension, which could lead in cell damage. In contrast, CT26 and NIH/3T3 cells required minimal resuspension.

The logarithmic growth phases of the cell lines are depicted in Figure A.2 in Appendix A, where the logarithmic cell population is plotted as a function of time. This data was used to calculate the DTs, for the different cell lines, and the results can be found in Table 4.1. All DTs are presented with the corresponding 95%CI. 4T1 and CT26 cells had fastest DTs at $14(12-16)$ hours and $14(13-15)$ hours, respectively. KPC cells were the TCs with the slowest DT at $17(15-19)$, and were also slower than the fibroblasts, NIH/3T3, which had DT of $16(15-17)$.

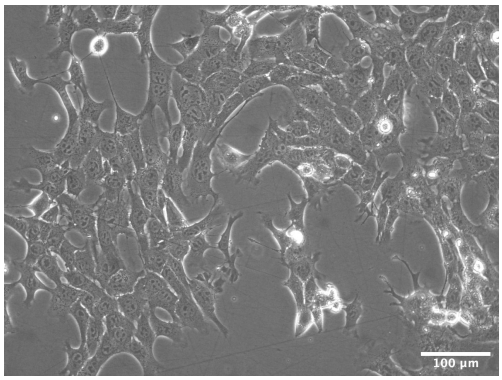


**(a)** 4T1 cells

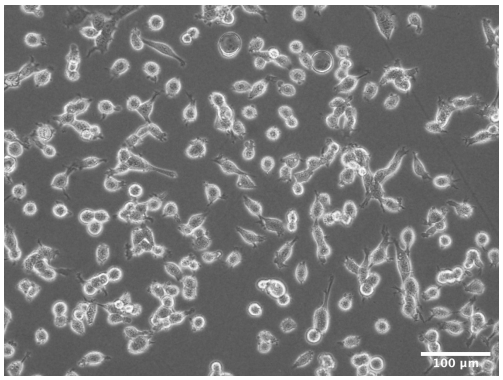


**(b)** CT26 cells

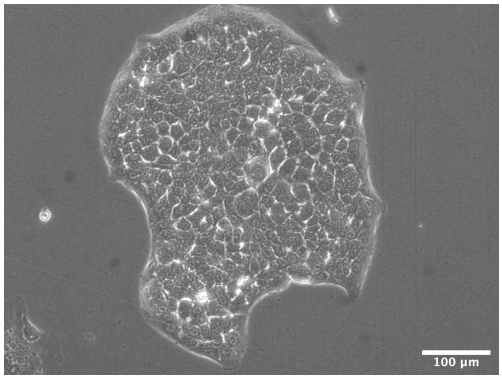


**(c)** KPC cells

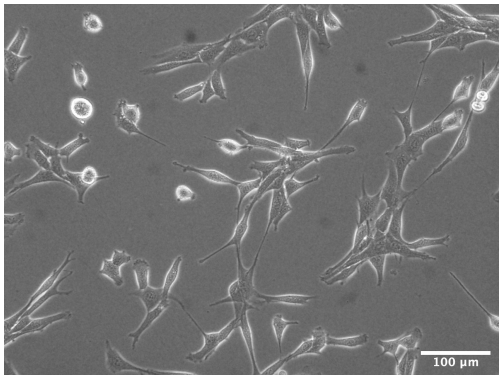


**(d)** NIH/3T3 cells

**Figure 4.1:** Phase contrast images showing the growth of tumor cells a) 4T1, b) CT26, and c) KPC, as well as fibroblasts d) NIH/3T3 in monolayer. Images are taken at $20X$ magnification and the scale bar indicates 100 µm.

**Table 4.1:** Cell line doubling times with 95% confidence intervals (95% CI): A comparative analysis of tumor cells 4T1, CT26, KPC, and fibroblasts NIH/3T3.

| Cell line | DT (h) | 95% CI (h) |
|---|---|---|
| 4T1 | 14 | 12-16 |
| CT26 | 14 | 13-15 |
| KPC | 17 | 15-19 |
| NIH/3T3 | 16 | 15-17 |

## 4.2 Growth of Multicellular Spheroids

In the result section, the spheroids are denoted with TC or F, depending on if they are cultivated in growth medium (GM) corresponding to the TCs or fibroblasts, respectively. Figure 4.2 shows the three different spheroid models in micro-wells at day 5 after seeding, cultivated in both F-GM and TC-GM. Variation in both size and sphericity between the spheroid models are observable from visual evaluation, but was also confirmed with quantitative analysis.

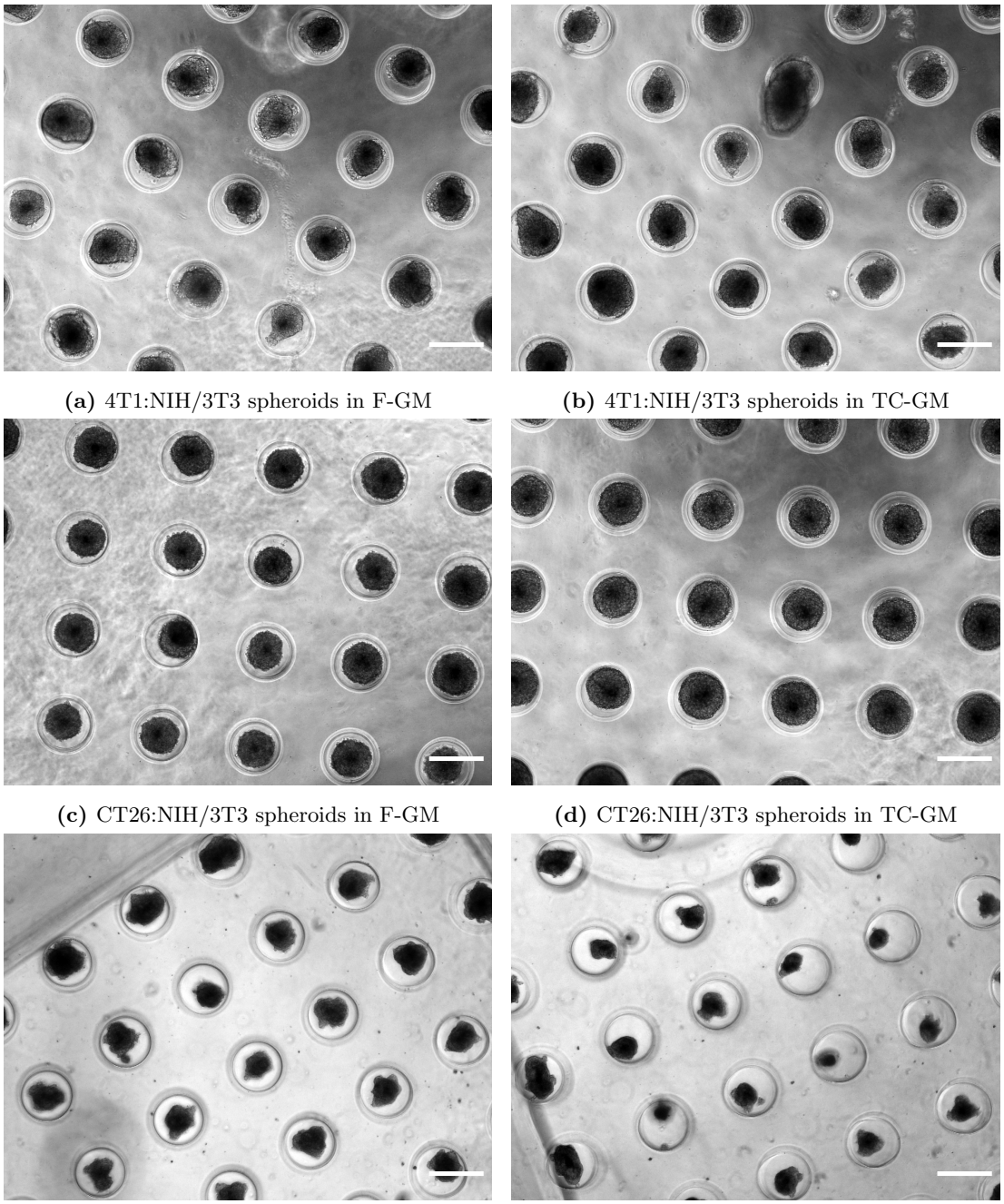

**(a)** 4T1:NIH/3T3 spheroids in F-GM

**(b)** 4T1:NIH/3T3 spheroids in TC-GM

**(c)** CT26:NIH/3T3 spheroids in F-GM

**(d)** CT26:NIH/3T3 spheroids in TC-GM

**(e)** KPC:NIH/3T3 spheroid in F-GM

**(f)** KPC:NIH/3T3 spheroid in TC-GM.

**Figure 4.2:** Various spheroids imaged at day 5 of cultivation in micro-wells. The scale bar indicates 400 µm

### 4.2.1 Volume-Doubling Time

Firstly, growth curves displaying the average spheroid volumes up to day 5 for all the spheroids in the two different GMs are presented in Figure 4.3. This reveals that CT26 MCSs obtained the largest volumes, 4T1 a little smaller, while KPC spheroids were the smallest MCSs of the group. 4T1 and KPC MCSs obtained larger volumes when cultivated in the F-medium, while for CT26 MCSs the opposite was observed. The time

it took for the spheroids to double in volume was measured in a similar manner as for growth in monolayers. The resulting V-DT, with corresponding 95% CI are presented in Table 4.2. CT26 MCSs grew the fastest, with no difference between the two GMs, with a V-DT of $1.4(1.3-1.5)$. 4T1 MCSs had V-DT in F-GM of $1.5(1.4-1.6)$ days compared to $1.7(1.6-1.8)$ days in TC-GM. The same trend was seen for KPC MCSs where the V-DTs were $2.4(2.1-2.6)$ and $3.6(2.9-4.8)$ days in F-GM and TC-GM, respectively. Significantly slower growth of the KPC MCSs compared to for the two other cell lines was observed.

**Table 4.2:** Measured doubling times for multicellular spheroids of different tumor cell lines in 1:5 ratio with NIH/3T3 fibroblasts, in either growth medium corresponding to the fibroblasts (F) of the tumor cells (TC).

| MCS | GM | DT (days) | 95% CI |
|---|---|---|---|
| 4T1:NIH/3T3 | F | 1.5 | 1.4-1.6 |
| 4T1:NIH/3T3 | TC | 1.7 | 1.6-1.8 |
| CT26:NIH/3T3 | F | 1.4 | 1.3-1.5 |
| CT26:NIH/3T3 | TC | 1.4 | 1.4-1.4 |
| KPC:NIH/3T3 | F | 2.4 | 2.1-2.6 |
| KPC:NIH/3T3 | TC | 3.7 | 2.9-4.8 |

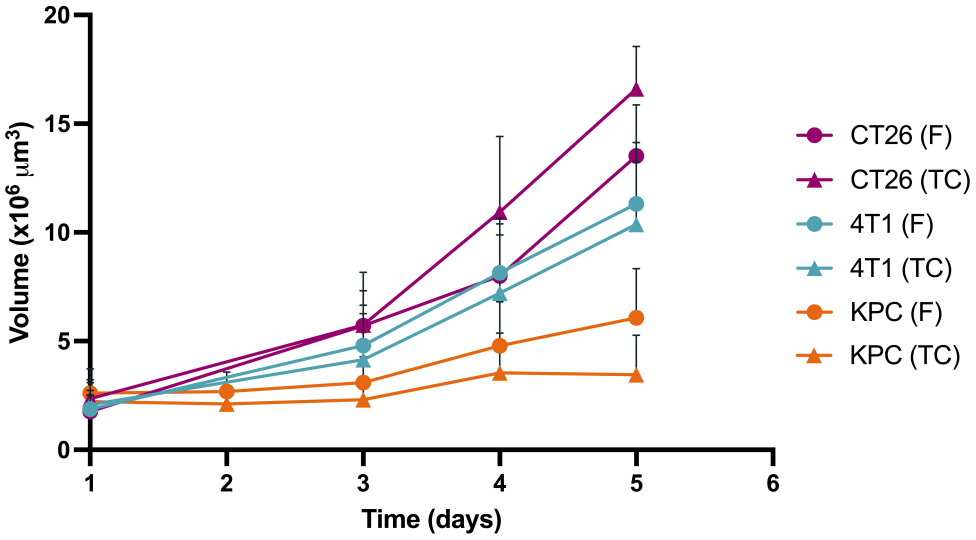


**Figure 4.3:** Growth curve of multicellular spheroids. Each point represents the average volume of around 40 spheroids, error bar represents standard deviation (SD) (only showing positive SD for readability). Spheroids grown in fibroblast (F) growth medium is marked with circles (●), and tumor cell (TC) growth medium is marked with triangles (▲).

### 4.2.2 Volume and Sphericity at Day 5

Figure 4.4 presents the volumes and sphericity of the spheroids on day 5 after seeding.

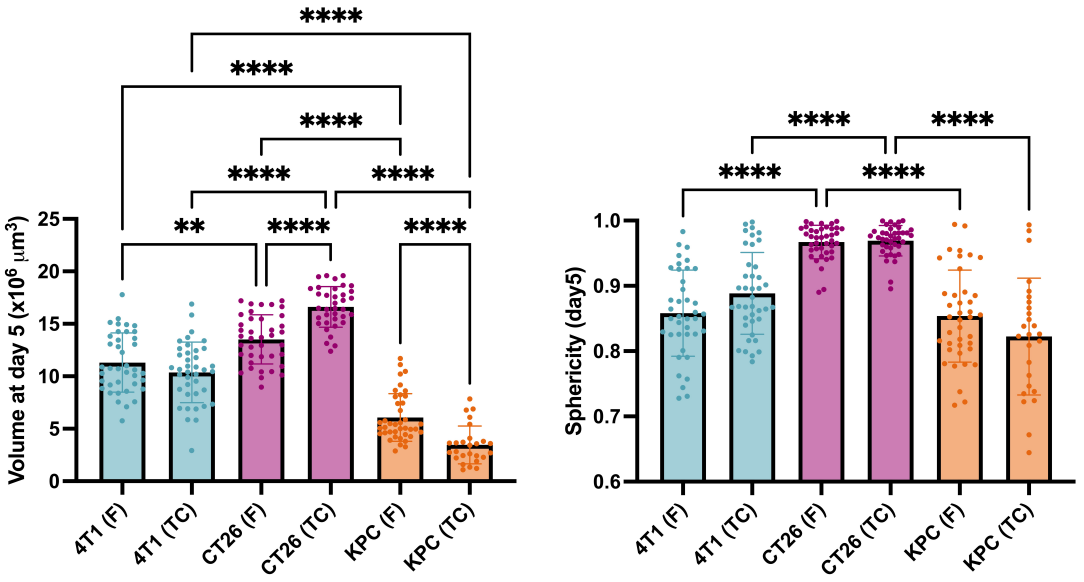


**(a)** Volume **(b)** Sphericity

**Figure 4.4:** a) Volume and b) sphericity distribution at day 5 of growth for spheroids in different growth medium, either belonging to the tumor cell line (TC) or the fibroblasts (F). Each point represents a single spheroid, and each bar represents the mean of 40 spheroids. **** indicates p-values $< 0.0001$.

#### Volume

As seen in Figure 4.4a, CT26 MCSs obtained the largest volumes with mean values of $17 \pm 2 \times 10^6 \mu m^3$ and $14 \pm 2 \times 10^6 \mu m^3$, for MCSs in TC-GM and F-GM, respectively. 4T1-TC and 4T1-F MCSs obtained means of $11 \pm 3 \times 10^6 \mu m^3$ and $8 \pm 3 \times 10^6 \mu m^3$. The MCSs of smallest volumes were KPC-TC and KPC-F with $4 \pm 2 \times 10^6 \mu m^3$ and $5 \pm 2 \times 10^6 \mu m^3$. The CT26 MCSs grew significantly larger in TC-GM, while KPC the opposite was observed. There was no significant difference for the 4T1 MCSs. For the KPC MCSs this aligns with the trend of the V-DTs, but not for the other two spheroid models.

#### Sphericity

The sphericity was calculated based one the difference between the two radii, $a$ and $b$, and is given as a number between 0-1, where 1 signifies a perfect sphere with $a = b$. Variations in sphericity between the MCSs at day 5, are displayed in Figure 4.4b. CT26 MCSs, that was found to be the largest, was also found to have the highest sphericity, while 4T1 and KPC MCSs were less spherical. CT26-TC and CT26-F had

mean sphericities of $0.97 \pm 0.023 \times 10^6 \mu m^3$ and $0.97 \pm 0.026 \times 10^6 \mu m^3$, revealing very high degree of symmetry. With intermediate degree of sphericity was 4T1-TC and 4T1-F MCSs, that had means of $0.89 \pm 0.063 \times 10^6 \mu m^3$ and $0.86 \pm 0.066 \times 10^6 \mu m^3$. Finally, KPC-TC and KPC-F had the lowest of means of sphericity at $0.082 \pm 0.089 \times 10^6 \mu m^3$ and $0.85 \pm 0.070 \times 10^6 \mu m^3$, respectively. Significant differences was found for CT26-F with both 4T1-F and KPC-F, and similarly for CT26-TC with 4T1-TC and KPC-TC. No statistically significant differences in sphericity between MCSs of the same cell line, in different mediums, were found.

## 4.3 Cellular Organization within MCSs

For the following experiments, the TC-GM to the corresponding MCSs was used for cultivation. A selection of CLSM images that displays the distribution of fibroblasts (green) and TCs (blue) withing MCSs can be seen in Figure 4.5. The organisation within 4T1 (a-c) and CT26 (d-f) MCSs is similar, with TCs and fibroblasts being mixed within the spheroids. In some cases, 4T1 MCSs seemed to have a more distinct separation of the different cell types, with fibroblasts highly localised in the periphery of the spheroid, while CT26 MCSs were observed to have an overall more homogeneous distribution. Interestingly, in KPC MCS (g-i) TCs and fibroblasts were completely separated and formed multiple smaller TC monospheroids attached to one larger monospheroid consisting of fibroblasts.

Data analysis confirmed these observations, by quantifying the percentage of the total TCs and fibroblasts in the spheroids that are located in the periphery. The results are presented in Figure 4.6. The sample size for each data set is 3, and it is the images in Figure 4.5 that was included in the analysis. Both 4T1 and CT26 MCSs had a larger portion, between $60 - 70\%$, of their fibroblast located in the periphery. The difference between the two spheroid types was within the distribution of TCs, where CT26 had a significantly higher percentage in the periphery than 4T1. KPC MCSs had the opposite distribution where fibroblasts were almost exclusively located in the center of spheroids, and the TCs in the periphery. In addition, while 4T1 and KPC had a significantly higher amount of fibroblasts than TCs in the periphery, the difference between the two cell types was not significant for the CT26 MCSs.

Differences of statistical significance as of the amount of TC and fibroblasts in the periphery within the same spheroid model was only found for 4T1 and KPC. Data used for the calculations can be found in Table **??** in Appendix **??**.

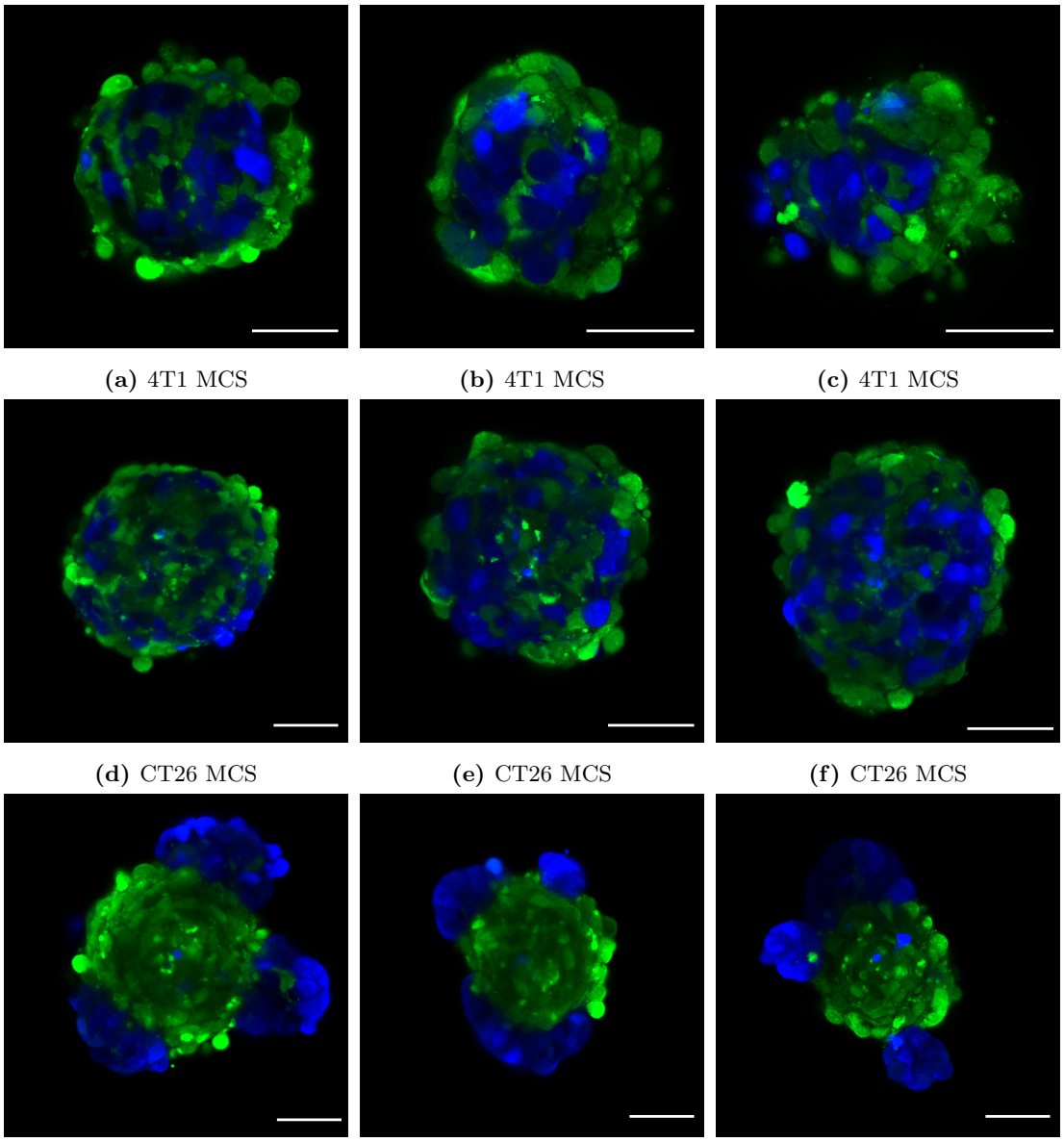

**(a)** 4T1 MCS **(b)** 4T1 MCS **(c)** 4T1 MCS

**(d)** CT26 MCS **(e)** CT26 MCS **(f)** CT26 MCS

**(g)** KPC MCS **(h)** KPC MCS **(i)** KPC MCS

**Figure 4.5:** Selection of CLSM images of multicellular spheroids in 1:5 ratio of tumor cells (blue), 4T1 (a-c), CT26 (d-f), and KPC (g-i), and fibroblasts NIH/3T3 (green) Scalebar represents 50 µm. Day 2 after seeding.

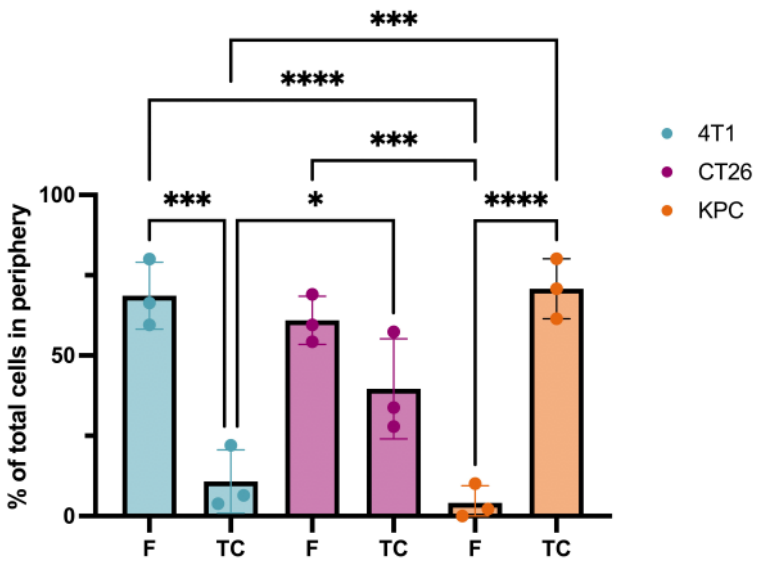


**Figure 4.6:** Percentage of total tumor cells and fibroblasts within different spheroids that are located in the periphery. The sample size of each variation is 3 spheroids, where each data point is represented by a circle. Standard deviations are represented by bars. Statistical significance is indicated by stars ($* : \leq 0.05, ** : \leq 0.01, *** : \leq 0.001, and **** : \leq 0.0001$).

## 4.4 Collagen and sGAG contents within MCSs of different cell lines

Absorbance measurements calculated the concentration of collagen and sGAG in the samples. Concentrations were adjusted for any dilutions during the essay and the final contents were given in $\mu g\, mg^{-1}$ MCSs. Sample size for collagen measurements is $n = 2$, with 1 replica per sample. For sGAG it was $n = 1$, with 2 duplicates per sample samples. For sGAG measurements in 4T1 MCSs, $n = 3$ the measurement from the test run also was included.

Average collagen and sGAG contents are found Figure 4.7. Collagen contents were found the be 1000× lower than sGAG contents in the spheroids. MCSs of 4T1, CT26, and KPC had average collagen contents of $0.03 \pm 0.01$, $0.03 \pm 0.02$, and $0.04 \pm 0.00$, respectively. Average sGAG contents were found to be $2.08 \pm 0.56$, $2.07 \pm 0.33$, and $1.89 \pm 0.40$. Due to small sample sizes, no differences of statistical significance was found.

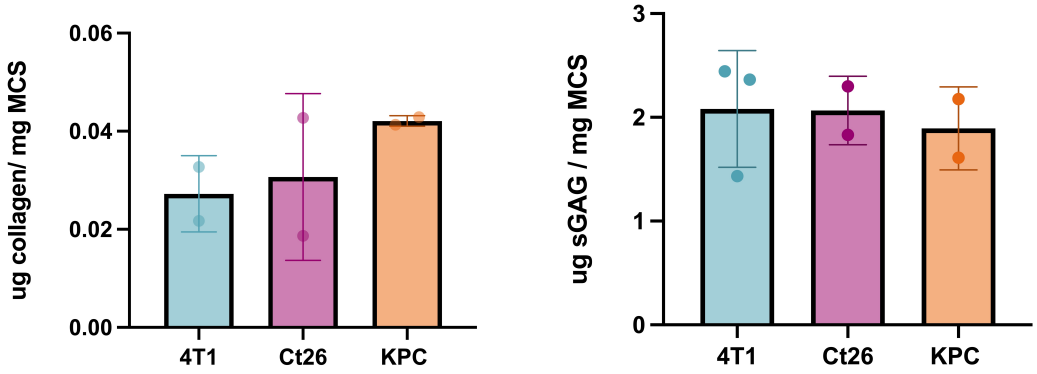


**(a)** collagen contents

**(b)** sGAG contents

**Figure 4.7:** Measured a) collagen and b) sGAG contents in three different multicellular spheroid models.

## 4.5 Nanoparticle uptake within MCSs

To measure NP uptake and penetration into MCSs, spheroids were harvested after 2 days and left to incubate with NPs on a mechanican roller for 3, 6, and 24 hours. Different sample tubes were created for each variation of MCS, NP size, and time point. This means that the MCSs imaged at one time point is different from the other time points, and it was not possible to observe the uptake of the same MCS over the full time period. For the data analysis in Matlab, the images (only NP channel) were thresholded. An excerpt of the thresholded images is included in Figures 4.8-4.10, and shows the NPs distribution within the MCSs.

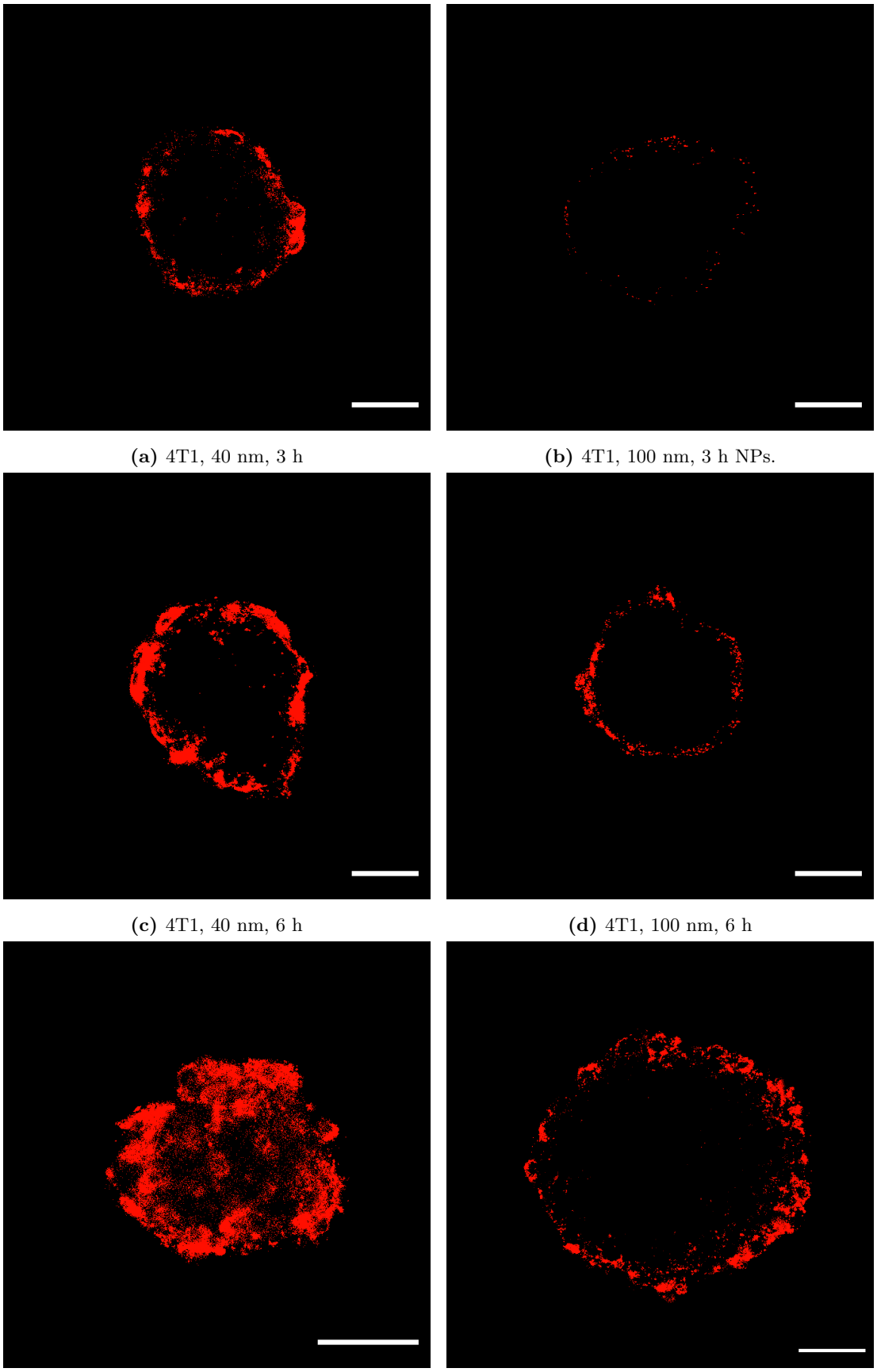

**(a)** 4T1, 40 nm, 3 h

**(b)** 4T1, 100 nm, 3 h NPs.

**(c)** 4T1, 40 nm, 6 h

**(d)** 4T1, 100 nm, 6 h

**(e)** 4T1, 40 nm, 24 h

**(f)** 4T1, 100nm, 24h

**Figure 4.8:** Thresholded images of nanoparticles (NPs) located in 4T1 multicellular spheroids after different incubation times. NPs of 40 nm are in (a,c,e,) while (b,d,f) shows 100 nm.

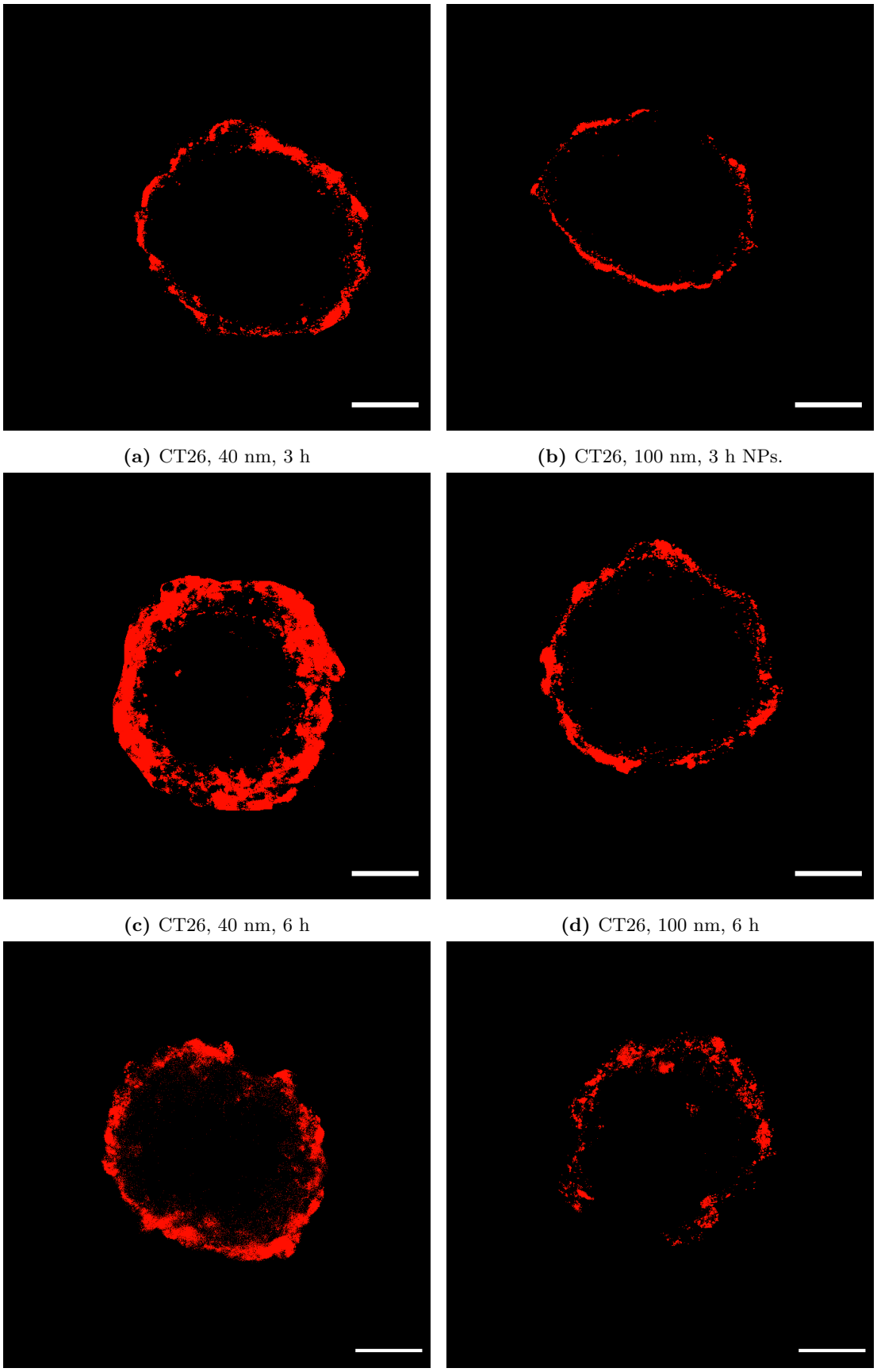

**(a)** CT26, 40 nm, 3 h

**(b)** CT26, 100 nm, 3 h NPs.

**(c)** CT26, 40 nm, 6 h

**(d)** CT26, 100 nm, 6 h

**(e)** CT26, 40 nm, 24 h

**(f)** CT26, 100nm, 24h

**Figure 4.9:** Thresholded images of nanoparticles (NPs) located in CT26 multicellular spheroids after different incubation times. NPs of 40 nm are in (a,c,e,) while (b,d,f) shows 100 nm.

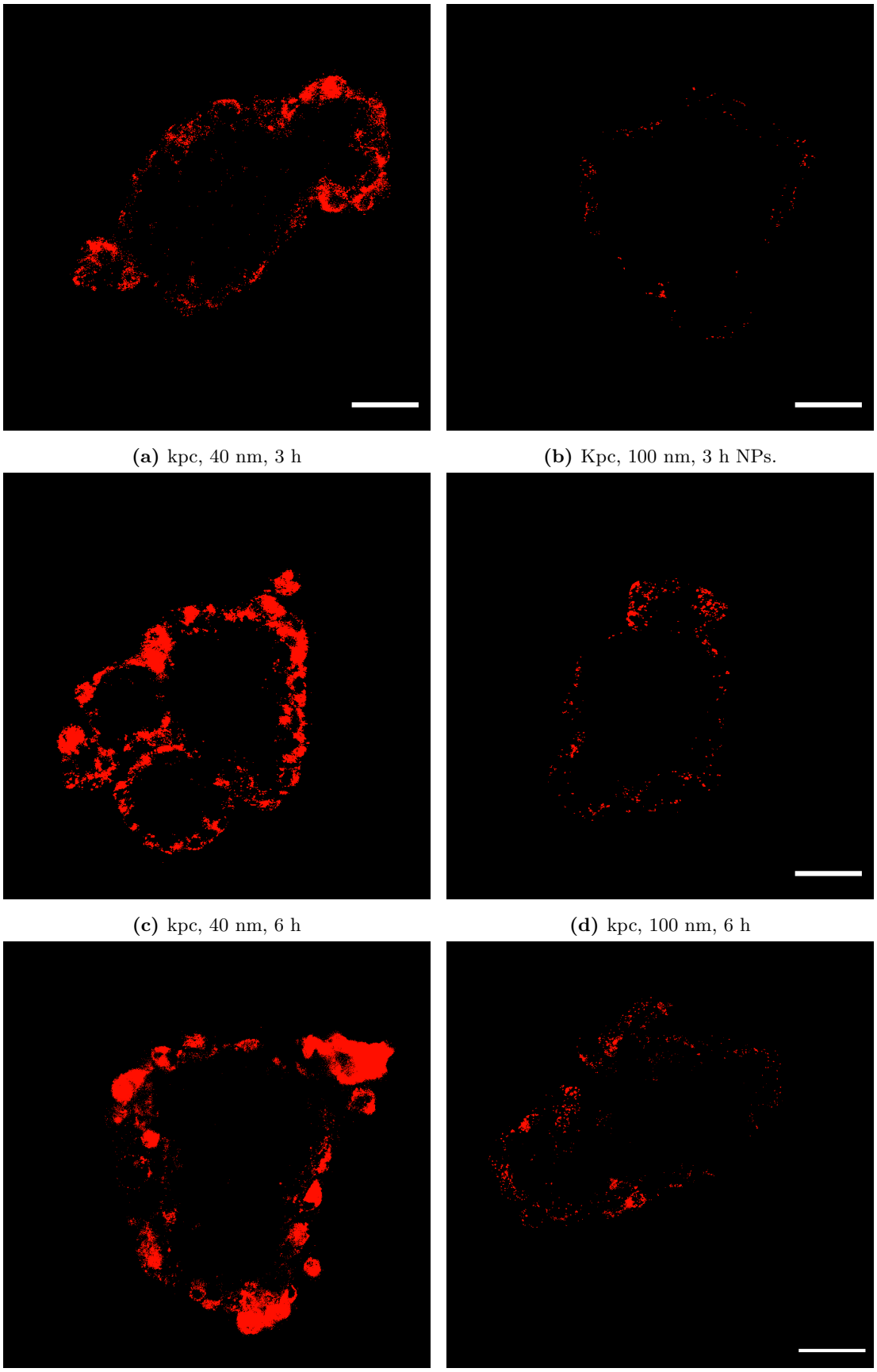

**(a)** kpc, 40 nm, 3 h

**(b)** Kpc, 100 nm, 3 h NPs.

**(c)** kpc, 40 nm, 6 h

**(d)** kpc, 100 nm, 6 h

**(e)** kpc, 40 nm, 24 h

**(f)** kpc, 100nm, 24h

**Figure 4.10:** Thresholded images of nanoparticles (NPs) located in KPC multicellular spheroids after different incubation times. NPs of 40 nm are in (a,c,e,) while (b,d,f) shows 100 nm.

### 4.5.1 Effect of NP size on penetration ability over time

Figure 4.11 illustrates the normalized total uptake in each of the spheroid models. The trends for the two NP sizes are the same, with highest uptake in CT26 MCSs, followed by 4T1 MCSs, and the lowest uptake in KPC MCSs.

More detailed graphs, illustrating the NP distribution within each MCS for all time points, 3, 6, and 24 hours, are in Figure 4.12 (4T1 (a-b), CT26 (c-d), and KPC (e-f)). Each data point represents the average intensity at a particular distance from the MCSs boundary, where the intensity values are proportional to the amount of particle present. The data sets have varying sample size, $n$, as noted in the graph legends. Absolute intensities are comparable only between graphs with same NP size, as different imaging settings was used for the two different NPs.

In general, the trend is increasing penetration depths with time, as well as larger penetration for the smaller NPs. However, as can be observed also in the thresholded images, the penetration into the core of the MCS is generally poor, and NPs are highly accumulated in the periphery of the MCSs. Still, for CT26 and KPC MCSs, for 40 nm, and for 4T1 MCSs for both sizes, there seems to be both increased penetration depth, as well as intensities, over time. In contrast, as observed in Figure 4.12 the penetration depth into CT26 (d) and KPC (f) MCSs for 100 nm seems to be relatively constant and time independent.

Another observation is that CT26 MCSs have a higher uptake of NPs after 3 hours than the other MCSs, especially noticeable for the 100 nm NPs (Compare subfigure (b) in Figures 4.8-4.10 and subfigures (b, d, f) in Figure 4.12. While the NPs are barely noticeable for 100 nm after 3 hours for the other cell lines, they are clearly visible for CT26.

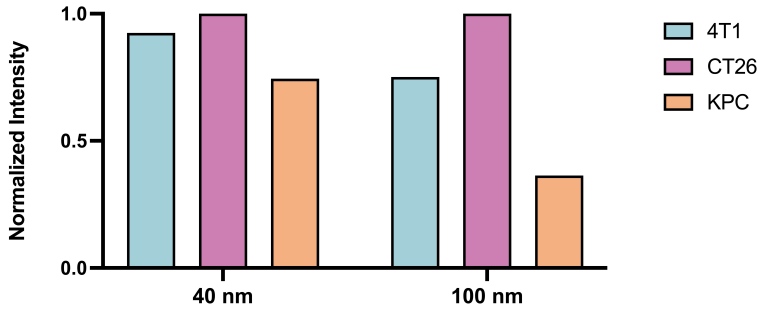


**Figure 4.11:** Sum of average total uptake into multicellular spheroids for all time points, 3, 6, and 24 hours. Separate normalization of the 40 nm and 100 nm uptake was done.

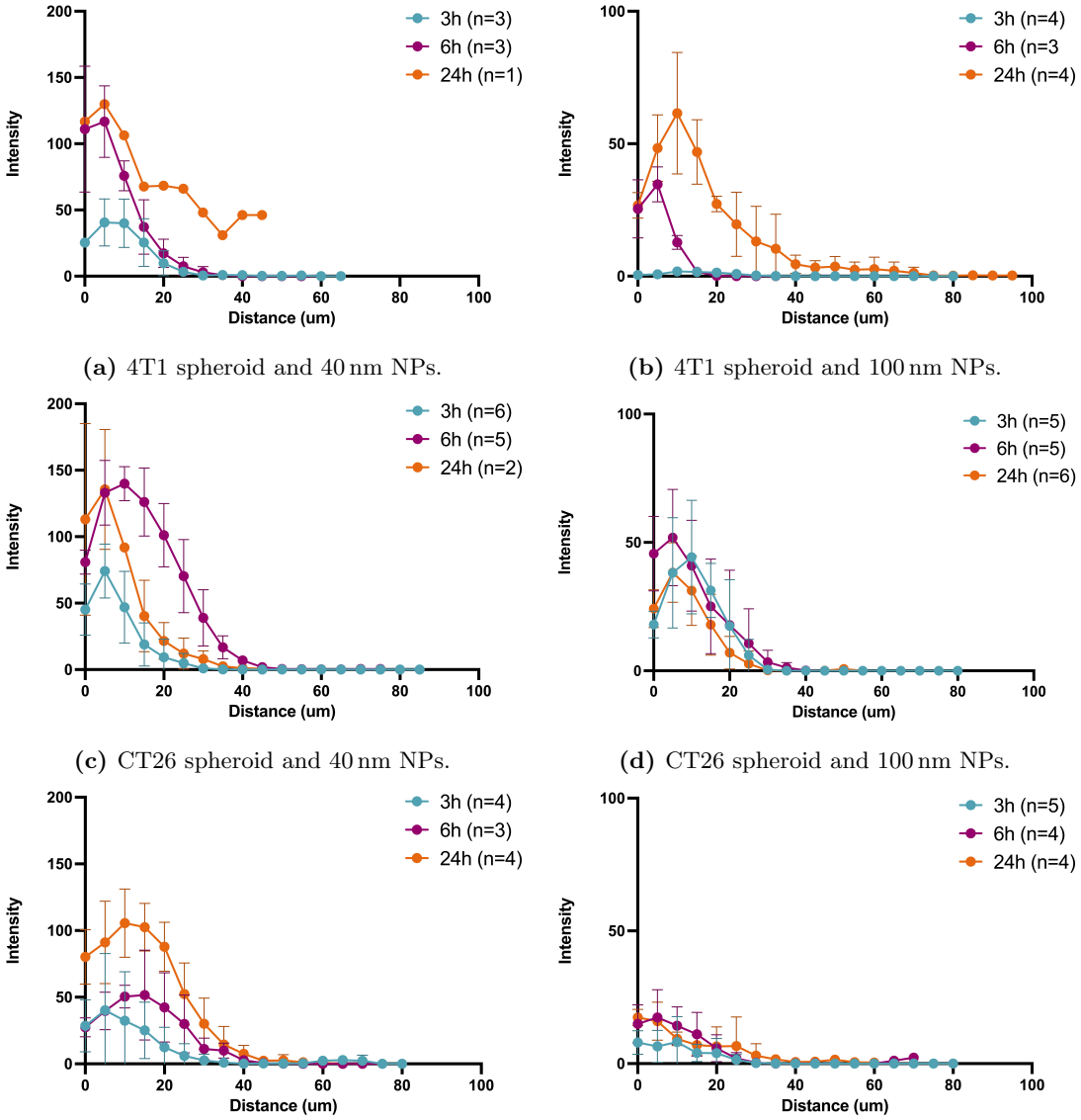


**(a)** 4T1 spheroid and 40 nm NPs.

**(b)** 4T1 spheroid and 100 nm NPs.

**(c)** CT26 spheroid and 40 nm NPs.

**(d)** CT26 spheroid and 100 nm NPs.

**(e)** KPC spheroid and 40 nm NPs.

**(f)** KPC spheroid and 100 nm NPs.

**Figure 4.12:** Average Nanoparticle (NP) uptake at different distances within multicellular spheroids (4T1, CT26, KPC in 1:5 ratio with NIH/3T3), illustrating penetration abilities of NPs of different sizes in different spheroid models. Uptake is measured seperately for 3, 6, and 24 hours. Each data point represent the average measured intensity for varying sample size, $n$, given in the legends. Standard deviation is represented with errorbars.

### Spatial distribution of NPs after 6 hours

Figure 4.13 gives relative intensities (fraction of the total intensity in the MCS) for the different MCSs after 6 hours. A larger portion of the 100 nm particles were located at the periphery of the spheroid compared to the 40 nm particles. This was the trend for all three spheroid models.

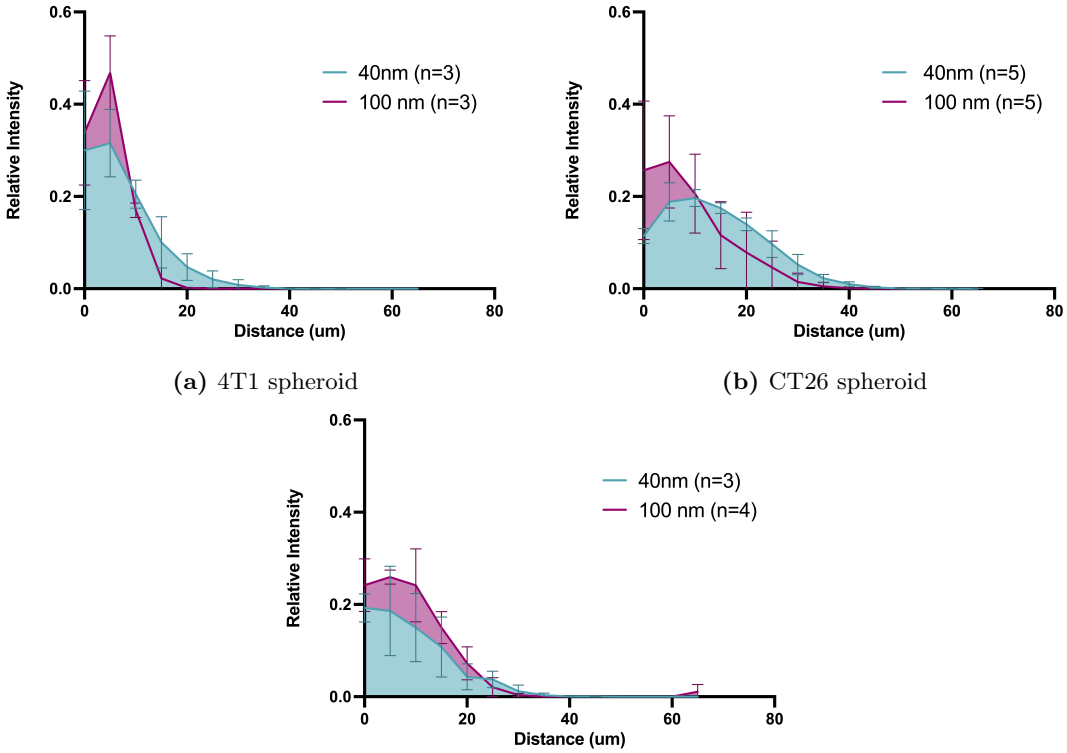


**(a)** 4T1 spheroid

**(b)** CT26 spheroid

**(c)** KPC spheroid

**Figure 4.13:** Relative intensities representing fraction of nanoparticles at each distance from the boundary of the spheroids after 6 hours. The different spheroid models are shown in separate subfigures a) 4T1, b) CT26, and c) KPC.

### Temporal evolution of uptake at fixed distance

Figure 4.14 shows the intensities of NPs at a fixed distance of 10 µm from the boundary of the spheroid, as a function of time.

When comparing the spheroid models in Figure 4.14a, 4T1 MCSs has a higher uptake rate from 3 to 6 hours, whilst in KPC MCSs most of the uptake occur between 6-24 hours. CT26 has a very high increase in uptake from 3 to 6 hours before there is a decrease in intensity at 24 hours.

For 100 nm, in Figure 4.14b, both 4T1 and KPC MCSs has very little uptake from 3 to 6 hours, and whilst 4T1 has a large increase in uptake up to 24 hours, KPC has a decrease. For CT26 MCSs the highest average uptake at this distance within the MCSs is at 3 hours, and it steadily decreases until the minimum average uptake at 24 hours.

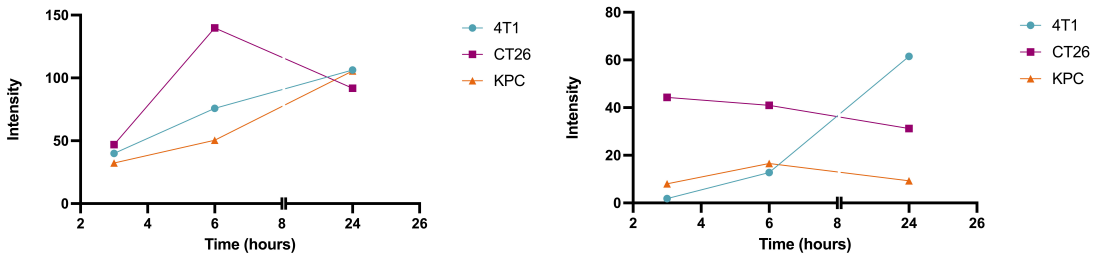


**(a)** 40 nm nanoparticles

**(b)** 100 nm nanoparticles

**Figure 4.14:** Nanoparticle uptake at 10 µm distance within the spheroids as a function of time.

### 4.5.2 Variation in cellular uptake between TCs and fibroblasts

.

In CLSM images ($\Delta z = 50\,\mu m$) in Figure 4.15, all three components, TCs (blue), fibroblasts (green) and NPs (red) are visualized. As the cells are fluorescently labeled in the cytosol, any overlap with the NPs indicates that the particles have been taken up by the cell. By visual evaluation of Figure 4.15 a) and b), TCs seem to have higher uptake of NPs into the cells than the fibroblasts. In 4T1 MCSs in Figure 4.15c there is only fibroblasts in the periphery, and correspondingly the uptake is almost exclusively in fibroblasts.

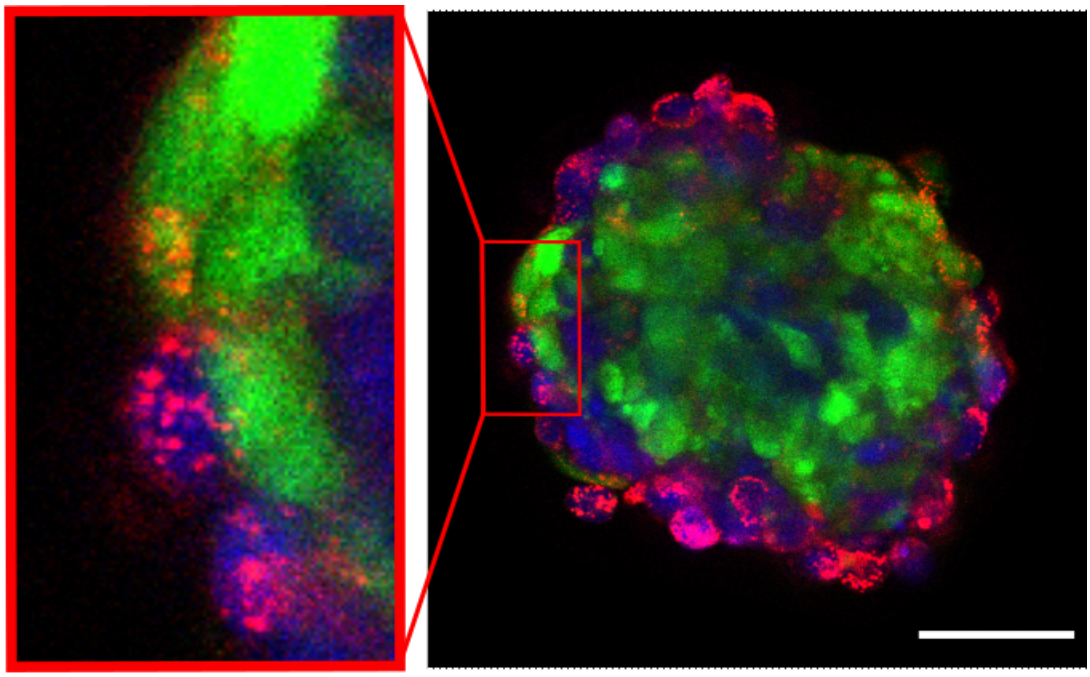

**(a)** CT26 MCS

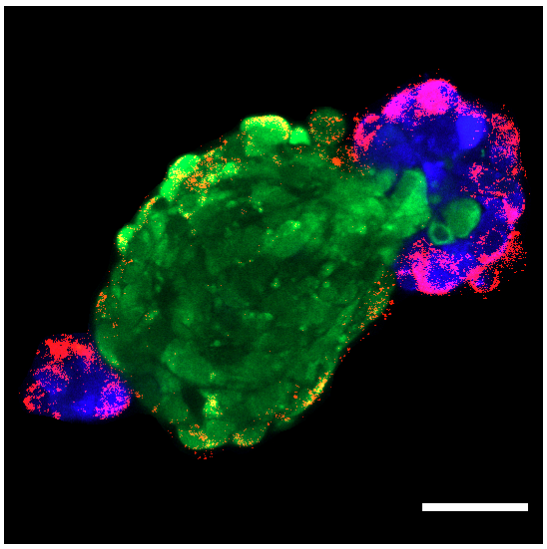

**(b)** KPC MCS

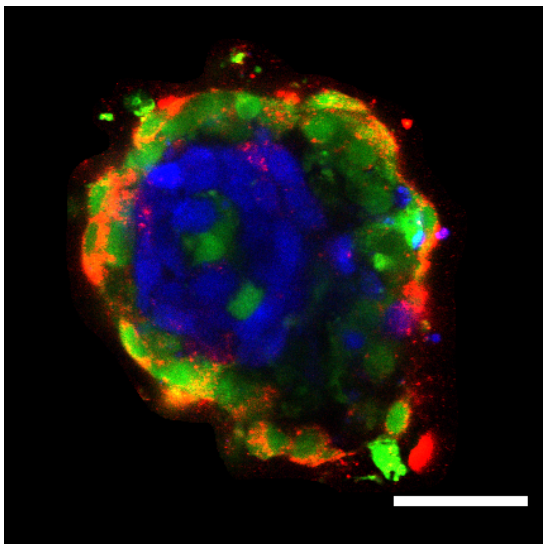

**(c)** 4T1 MCS

**Figure 4.15:** Confocal laser scanning microscopy (CLSM) images at depths, $\delta z$=50 µm within multicellular spheroids (MCSs). Tumor cells (4T1, CT26, KPC) are in blue, fibroblasts (NIH/3T3) are in green, and nanoparticles in red. Scale bar represents 50 µm.

### 4.5.3 Correlation between ECM Contents and NP Uptake

Plots showing the correlation between NP uptake in the different spheroid models and ECM contents are in Figure 4.16 (a) Uptake vs Collagen, b) Uptake vs sGAG). The uptake of NPs into the MCSs decrease with increasing contents of collagen with correlation coefficients, $r$, equal $-0.87$ and $-0.77$ for 40 nm and 100 nm particles respectively. In contast, the uptake increased with increasing content of sGAG, with $r$ equal to

0.93 and 0.86 for 40 nm and 100 nm particles respectively. Due to few data points, no statistically significant differences could be found.

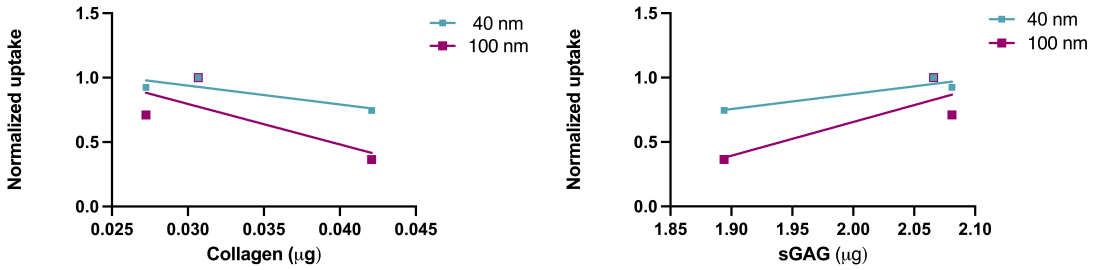


**(a)** 40 nm nanoparticles

**(b)** 100 nm nanoparticles

**Figure 4.16:** Correlation plots between NP uptake in various spheroids and ECM constituents contents. a) shows strong negative correlation between NP uptake and collagen contents in (40 nm, r=-0.87; 100nm, r=-0.77), and b) strong positive correlation between NP uptake and sGAG contents in spheroids. Non of the correlations were of statistical significance (40 nm, r=0.93 ; 100nm, r=0.86).

# Chapter 5

# Discussion

## 5.1 Growth and Morphology of Cells in Monolayers

Gaining an understanding of the distinctions among cell lines when cultivated in monolayers can provide valuable insight into their growth patterns in 3D cultures. In particular, the variations observed among the TCs can help explain the diverse properties they exhibit when cocultured with fibroblasts in MCSs.

### 5.1.1 Doubling Times

In the initial investigation of DTs for the different cells in monolayer culture, it was observed that 4T1 cells had the fastest DT, followed by CT26 NIH/3T3, and finally KPC, which was the slowest-growing cell line. Given that cellular growth is strongly influenced by the environment, it is valuable to assess cell growth under our laboratory conditions and compare it to reported findings in literature. The comparison offers insight into the comparability of our study results with those of others, providing a broader context for interpretation.

The estimated DT of 4T1 cells was 14 hours, which is in accordance to the reported DT of 12.6 hours from ATCC [52]. For CT26 cells, the measured DT was 14. While a directly comparable DT was not found in the literature, the similar cell line CT26.CL25 was reported to have a significantly higher DT of 22.2 hours [53]. For KPC, the seemingly slowest-growing cell line, the DT was 17 hours. Another study that measured DT in various KPC cell lines reported a range from 14-30 hours, highlighting the large variation also within similar cell lines. Our KPC cell line fell on the lower end of this spectrum. The NIH/3T3 cell line was estimated to have a DT of 16, which is lower than the the range reported in literature as 20-26 hours [54].

In conclusion, the measured DTs in this study were both lower and higher than those reported in other literature sources, showing no real trend. This could be due to

unavailable information for identical cell lines in certain cases, but also emphasizes the substantial variability in DTs.

### 5.1.2 Cell-Cell Interaction and CAM Expression

In this study it was revealed distinct differences in the morphology and growth patterns of the various cells lines examined when cultivated in monolayers. Specifically, the tumor cell lines 4T1 and KPC grew in clusters, and exhibited larger cell-cell contact areas compared to CT26. ATCC lists the CT26 cell line with fibroblastic morphology [55], but only some of the cells in the monolayers displayed the elongated and stretched out growth pattern similar to NIH/3T3. This elongated spindle-shaped appearance is a characteristic feature of fibroblasts, and other mesenchymal cells, enabling their contractile function and movement in response to stimuli.

The growth pattern observed in 4T1 and KPC cells, along with their difficulty in separation, suggests these cells have strong binding affinity among themselves. Differences in CAM expression, particularly the expression of E-cadherin, may contribute to the observed variations in cell-cell interactions. Other CAMs may be important, but for simplicity we will be focusing on comparing E-cad/N-cad due to their usage to mark EMT, and separate epithelial cells from mesenchymal cells. E-cadherin known to be abundant in epithelial cells and have high affinity for homophilic binding [16], is therefore hypothesized to be more abundantly expressed in 4T1 and KPC cells, leading to the high binding amongst cells. Whereas the low binding cell lines, CT26 and NIH/3T3, presumably have lower E-cadherin expression, and higher N-cadherin expression. Both fewer bindings, and weaker bindings are possible reasons that could lead to the fact that these cells are easily separated.

Previous studies have reported findings that support this hypothesis. Li et. al (2014) found that E-cadherin was homogeneously expressed in a wide range of independent KPC cell lines [56]. Similarly, Lou et. al (2008) studied the metastatic 4T1 cell line in relation to different EMT markers, as EMT is linked to metastatic properties [57]. Surprisingly, 4T1 was found to express substantial amounts of E-cadherin both in in-vivo tumors and in-vitro monolayers which demonstrates maintenance of the epithelial morphology. In the same study, expression in NIH/3T3 was also investigated for comparison to a mesenchymal cell line. As expected, NIH/3T3 did not express E-cadherin, but surprisingly not that high expression of N-cadherin either. Instead it had high levels of vimentin and other EMT markers. Other sources have since reported higher levels of N-cadherin in NIH/3T3 fibroblasts [58]. For simplicity, it will be assumed that NIH/3T3 are N-cadherin expressing. Lastly, Castle et.al (2014) reported no expressions of E-cadherins in the CT26 cell line, but high N-cadherin expression [59]. This is in agreement with the statement that CT26 have a mesenchymal morphology.

## 5.2 Growth Characteristics of MCSs

### 5.2.1 Cellular Organization within MCSs

All three spheroid models displayed differences in their distribution of fibroblasts and TCs within the MCSs. Although with different organization, a separation of the two cell types were observed in both 4T1 and KPC MCSs. For 4T1 it was the TCs in the center, with fibroblasts in the periphery. In KPC MCSs, the degree of separation was even higher. Rather than being enclosed within fibroblasts, the KPC cells formed entirely separate spheroids, only bound to the NIH/3T3 in small contact areas.

This organization is likely due to cell sorting phenomenon (also known as phase separation, or cell segragation) [60][61], that occurs between cell lines that exhibit different expression of CAMs (specifically E-cadherin and N-cadherin). The seemingly different expression of cadherins is therefore a plausible explanation for the observed differences. The concept of a "sphere within sphere", observed for 4T1 MCSs, was a cell sorting configuration introduced by Steinberg et. al (1994) [61]. It is explained as a phenomenon that occur when two cell types differ in their cell adhesion properties [61]. In this case it was the E-cadherin expressing in the center, with N-cadherin expressing NIH/3T3 cells in the periphery. They further lists two demands that needs to be present for this particular configuration to occur. Firstly, the cells that forms the medulla, here 4T1, must be the cells with the most cohesive properties. Secondly, the cells in the periphery need to adhere to the cells in the center (medulla) with an intensity equal to, or greater than, that which they adhere homotypically with. This implies that NIH/3T3 have equal or stronger affinity towards binding to 4T1 than they cells of their own kind.

As KPC MCSs exhibit cell sorting, but not in this same "sphere within a sphere" configuration, it is indicated that the two criteria is not met. From assessing the monolayer morphology it was assumed that KPC have higher cohesive properties than NIH/3T3. This implies a breach of the second criteria, and that both cells in this case have higher affinity for homotypical cell binding. As KPC is the most cohesive cell line of the two, it could be expected that that they would create the main spheroid, with NIH/3T3 spheroids attached to it. However, this is the opposite as what was observed. A possible reason could be the $1:5$ ratio of TCs and fibroblasts, and that the cell type in majority create the larger spheroids. This hypothesis could be tested by cultivating some KPC:NIH/3T3 spheroids in the opposite ratio $5:1$ to see if the organization switches.

For CT26 MCSs,it was observed that these spheroids were more uniform in their distribution than 4T1 and KPC, although in some MCSs it was observed some smaller monocell aggregates. The homogeneity can be attributed to the CAM expression in CT26 cells, which is similar to that of NIH/3T3, with low E-cadherin expression and higher N-cadherin expression.

Supporting these claims, Hazan et. al (1997) showed that N-cadherin expressing breast cancer cells coaggregated with N-cadherin-expressing fibroblasts-like cells in higher degree than those expressing E-cadherin [22]. In a more recent study, Lotsberg et. al (2022) reported higher degree of segregation in cospheroids of fibroblasts with epithelial TCs expressing than in those with mesenchymal-like TCs with greater phenotypic similarity to the fibroblasts. Similarly to this study, cospheroids with epithelial TCs obtained the "shpere within a sphere" configuration, while mesenchymal TCs were uniformly distributed across the spheroid. Interestingly, an opposite distribution was observed in which the fibroblasts formed the medulla of the spheroids, while the TCs occupied the periphery. However, it is important to note that the cell types used in that study differed from ours, and the difference is likely due to an opposite relationship the cohesive properties of the two cell types. Even more surprisingly, Priwitaningrum et. al (2016) that studied 4T1/3T3 MCSs observed the same distribution as Lotsberg and her colleagues [47]. Although NIH/3T3 and the 3T3 cell lines are not identical, they are very similar, and one could expect similar results when cocultured with 4T1 cells. While exact differences between 3T3 and NIH/3T3 is uncertain, Priwitaningrum et. al report that when cultivated as monospheroid, 3T3 was denser than 4T1, which still supports the proposed theory.

### 5.2.2 Variations in V-DTs, Volume and Sphericity

In addition to differences in the cellular organization within the MCSs, there was also observed variations in V-DT, and volume and sphericity of the MCSs at day 5 of cultivation.

The estimation of V-DTs for the MCSs of different TCs, revealed that CT26 was the fastest-growing MCSs, followed by 4T1 MCSs, while KPC MCSs grew significantly slower compared to the other two spheroid models. When comparing DTs of the cells in monolayer to V-DT of the corresponding MCSs, one can observe both similarities and differences in the trends. KPC is the tumor cell line that grows the slowest in both monolayer and as spheroids, while for 4T1 and CT26, the roles are reversed. Where 4T1 was the fastest growing cell line in monolayer, CT26 is the fastest growing as spheroids. In addition, the gap between V-DT of KPC MCSs to the MCSs of other cell lines are much larger the difference for DT in monolayers. It is concluded that DT of the cells in monolayer can have an effect on growth in MCSs, but there are effects that are more important (i.e expression profiles and cell sorting) when it comes to predicting the size of MCSs of different cell lines.

The V-DT for the spheroids was in the range $1.4 - 3.7$ days, compared to other studies that report V-DTs between 0.6-2.1 days [62] [63]. No data on these specific spheroid models was found, and different cell lines can have very different growth characteristics. However, differences in measurements techniques and methods, with varying accuracy can affect V-DT reported in literature and here.

### Volume at Day 5

At day 5 when end-volumes were measured, CT26 MCS were largest, followed by 4T1 MCSs, and lastly KPC MCSs, following the same trends as the V-DTs. Additionally, all the variations between spheroid models was found to be of statistical significance. The difference in cadherin expression for each cell line, and therefore also their cohesive properties, is suggested as an explanation for the variations in volume. Highly cohesive cells tend to form more compact aggregates leading to smaller spheroids than those of less cohesive cells. This is in agreement with our conclusions that the 4T1 epithelial cells with high degree of cell-cell binding resulted in smaller spheroids than the low binding mesenchymal-like CT26 cells.

That KPC MCSs that were much smaller than the two others, could also be explained by the cellular organization of the MCSs. As TCs and fibroblasts are completely separated, one can consider the growth of these MCSs as the growth of multiple monocellular spheroids instead of a single MCS. Monospheroids were not studied in this thesis, however in the specialization project of the author it was observed that 4T1 cospheroids grew significantly larger than their monospheroid counterparts. This was independent of the TC-to-fibroblast ratio, as both 1:1 and 1:5 ratios exhibited a similar increase in growth compared to the monospheroids. This suggests there is some growth stimulating phenomenon occuring in cocultures. A theory is therefore that the KPC spheroids grow smaller in size because they behave like multiple monospheroids instead of a single MCS. Some studies have findings that supports this, while others contradict. Priwitaningrum et. al (2016), also using 4T1 in combination with a 3T3 fibroblast reported homospheroids were smaller in size than heterospheroids [47]. Conversely, Alzeeb et. al (2022) reported that spheroids of the gastric tumor cell line they studies grew smaller in size and less compact as monocellular spheroids than in MCSs [64]. They however also reported strong attachment between the two cell types, which does not seem to be the case between NIH/3T3 and neither 4T1 and KPC. A general theory is that MCSs grow more compact than monospheroids if the two cell types have suitable CAM expression and affinity to heterotypic bindings.

### Sphericity at Day 5

Regarding the sphericity of the MCSs, CT26 MCSs were significantly more uniform than both the two other spheroid models. With values close to 1, an almost perfect spherical shape of these MCSs was confirmed. While no statistical significance between the two other models were found, 4T1 MCSs were overall more uniform than the KPC MCSs. The higher sphericity of the CT26 MCSs is not unexpected, as the spheroids have been proven to be more homogeneous and uniform in their cellular organization. Higher degree of cell sorting and monocellular aggregates within the MCSs could be expected to decrease the sphericity.

With this in mind, it could be expected even lower sphericity results for the KPC, as the two cell types are completely separated from each other. Also with visual evaluation of the phase contrast images of the MCSs during cultivation, they seem to have significantly lower sphericity than 4T1 MCSs. A reason for this not being conveyed in the data, is the method used for measuring the sphericity. Both the volume and sphericity calculations of KPC is assumed to be less accurate than for the other spheroids, as the calculations assumed spheroids with high sphericity. The multiple smaller spheroids in the KPC MCSs were not accounted for, as both measurements were only based on the two perpendicular radii. This is a good method for oblate spheroids with relatively even surfaces, like 4T1, but fail to accurately describe spheroids with morphology similar to KPC MCSs. Another method could have been used that account for this by measuring the sphericity based on area to perimeter ratio rather than the radii.

### 5.2.3 Effect of Choice of Growth Medium

So far, we have only discussed the variations between spheroid models. A goal in the investigation was also to determine if the choice of GM had any implications on the growth of the MCSs. For the sphericity there was no statistically significant effect of the GM. However, for volumes at day 5, KPC-TC were significantly smaller than for KPC-F.

This can be a indicator that the NIH/3T3 cells are dissatisfied in the KPC TC-GM. Since 4T1 and CT26 have the same TC-GM, Looking into the ingredients and additatives in the three different mediums it is revealed that, compared to the two other GMs, the Dulbecco's Modified Eagle Medium (DMEM 1X) used in KPC are missing sodium pyrovate. Sodium pyruvate are often added to GMs as it is a good source of carbon, but it is not required in all cell cultures as it is normally produced as an intermediate metabolite by cells in the glycolysis pathway [65]. However, it is stated that when cultured with sodium pyruvate the cells can be dependent on it, and in the case of a sudden withdrawal it can cause a lag in cell growth. Consequently, when NIH/3T3 cells, that normally were cultivated in a sodium pyruvate positive medium, were brought into the sodium pyruvate negative medium of KPC they needed time to adjust to the new medium which again affected their growth. This is a viable explanation for the observed smaller average volumes and growth of KPC MCSs in TC-GM than F-GM. For potential future experiments with KPC:NIH/3T3 spheroids it would be recommended to add sodium pyruvate in the KPC TC-GM to avoid this issue. Another possible solution is to use the F-GM for the MCSs instead, as non of the cell lines seemed to react badly to this. Additionally, the latter suggestion would also increase the consistency between culturing conditions that increase the comparability between them.

The other difference was that CT26-TC grew significantly larger than CT26-F. RPMI-1640 medium contained HEPES which was not present in the other two GMs, but no

information was found that would explain the difference in growth. However as there is only an effect on the CT26 MCSs, a hypothesis is that NIH/3T3 cells grow as normally in the TC-GM, and instead it is the growth of the CT26 cells that are affected by the F-GM.

## 5.3 ECM Contents

ECM assays were performed on MCSs that were harvested after 2 days of growth, and with absorbance measurements collagen and sGAG contents were measured. The collagen contents were found to be very low in all of the MCSs. Although not significant, the KPC MCSs had a slightly higher average than for the two other spheroid models, while there was essentially no difference between contents in 4T1 and CT26 MCSs. For sGAG, variation in content between the different cell lines. No statistical significant differences were found sGAG either, but KPC MCSs had a slightly lower average than the two MCSs. This means KPC was found to be the spheroid model with both highest collagen content, and lowest sGAG content. Additionally, overall sGAG contents were 100 times higher than for collagen.

### 5.3.1 Comparison to In-Vivo Tumors

In tumors, the ECM components are typically produced by the stromal cells, specifically fibroblasts, of the host. However, the TCs have the ability to influence the rate of synthesis to create a favourable environment for their own growth and progression [66] [67](+ FInn nyere kilde?). Tumor cells have been proven to synthesize ECM constituents themselves, especially in an 3D environment, in an intermediate level between monolayers and tumors [62]. Consistently with this, the collagen and sGAG values are lower than those found previously in tumors grown with the same cell lines [49]. While no statistical significant difference for sGAG measurements between the tumor models were found, CT26 samples had significantly less collagen contents than the two other models. This was not the trend in MCSs, however more data is needed to gain more accurate results for MCSs. Furthermore, the collagen levels in tumors were significantly higher than the sGAG levels which is the opposite of what was observed in the MCSs. In other studies comparing ECM contents in spheroids to those in in-vivo tumors, it has been noted that variations observed among cell lines in the in-vivo setting are not maintained in in-vitro cultures [62] [67]. These findings align with the results presented in this thesis, as no statistically significant differences were found in neither the collagen nor the sGAG contents of MCSs.

### 5.3.2 Comparison to Monocellular Spheroids

In a previous study by Davies et. al (2002), collagen and sGAG levels were assessed in monospheroids [67]. Consistently with our measurements, they observed higher sGAG levels compared to collagen, although with a much smaller difference than the one observed in the current project. Therefore, the general trend seems to be that in spheroids (mono-/multicellular) sGAG contents are higher than collagen contents, while in tumors the opposite is observed. Notably, the collagen levels they reported were in the same range as to those detected in the MCSs of this study, while their sGAG levels were approximately 10 times lower. This is partly as expected, as it is anticipated that the presence of fibroblasts in MCSs would result in significantly higher ECM contents compared to fibroblast-free spheroids.

One possible explanation for the absence of the expected differences in collagen levels could be the disparity in cultivation time prior to spheroid harvesting. Davies et. al harvested their spheroids after a 5-day period, whereas in this study, the MCSs were collected after only 2 days. Consequently, it is plausible that a more prolonged lag phase in collagen production, in comparison to sGAG, may contribute to this outcome. However, no literature was found on this topic.

Also worth mentioning is that the collagen assay required a certain amount of collagen for accurate measurements, where the collagen measured has to be within the range of the standard curve. Our collagen samples did not meet these criteria, which makes the resulting concentration from the absorbance measurements unreliable. The detection limit for the collagen assay is normally 2.5 µg/100 µL. With the concentration & isolation step, collagen at concentrations 1.0 µg/100 µL can be measured [50]. The values obtained from the absorption measurements was below this, which means the results from the collagen measurements are not reliable. These measurements should be redone, and it should be considered to increase the number of cells/MCSs per sample. Instead of further increasing the number of cells seeded in each agar flask, it could be solved by collecting the pellets of multiple flasks and combining them before continuing with the assay.

## 5.4 Penetration and uptake of nanoparticles in MCSs

Understanding the kinetics of NP uptake and penetration in MCSs is crucial for the evaluation and further development of MCSs as a method for drug delivery studies. By measuring the uptake of NPs at different times and utilizing NPs of two different sizes, insight was gained into the time-dependent behaviour and size-dependent characteristics of NPs uptake in these specific spheroid models.

### 5.4.1 Temporal Evolution of Uptake in MCSs

When investigating the development of NP uptake over time, at a fixed distance of 10 µm into the MCS, two different trends were observed. The first one was as expected, a constant increase in fluorescence intensity over time, where the lowest intensity was measured for 3 hours and the highest after 24 hours. This was the case for the 4T1 MCSs for both NP sizes, as well as for KPC MCSs only for 100 nm NPs. Unexpectedly, for the rest of the MCSs the trend was maximum uptake at 6 hours followed by a decrease until 24 hours.

A possible reason for this could be a weakening of the signal at the 24 hour mark, due to a contamination in the sample. Some type of bacterial infection, that unfortunately was not uncovered until after the initiation of the MCSs, was present in some of the samples. It was originally only observed in the 4T1 cells, but at the 24 hour time point it was also observed a significant amount of bacteria in the CT26 samples. This cross-over is thought to be due to a transfer of bacteria from shared equipment across cell cultures during the harvesting and sample preparation process. It is not known exactly how this would affect the MCSs and uptake, but during imaging it could seem that the contamination to some extent interfered and subdued the intensity of the fluorescent signals, which made it challenging to take high quality images.

However, the fact that the 4T1 samples that were also contaminated do not share the trend of a decrease in uptake over time, weakens the credibility of this hypothesis. Moreover, an alternative suggestion is that this decrease is due to a change in the culture conditions following the infections that lead to damaged cells. As CT26 MCSs seemingly have a higher percentage of their TCs in the periphery compared to the 4T1 MCSs, a higher sensitivity to the infection in TCs than in the fibroblast could explain this discrepancy.

### 5.4.2 Effect of NP Size on Uptake in MCSs

There is a clear difference in uptake between the two different particle sizes, with better penetration for 40 nm than 100 nm. This is as expected as the ability of a particle to distribute though ECM via diffusion processes is highly related to its size. Because of their small size, drugs normally display easy entry into cells and traversal through the ECM. On the other hand, because of their larger size, NPs are anticipated to be more restricted in their movement through the ECM [68]. For the 100 nm NPs this is consistent with the results of other studies. Tchoryk et. al (2019) measured penetration and uptake in spheroids of NPs of varying size and surface properties [68]. Similarly to here, they reported that NPs of this size were strongly associated with the periphery of the spheroids. However, smaller particles (30-50 nm), were able to penetrate successfully at the core, with NP uptake in over 90% of the cells in the spheroid already after 6 hours. This is of large contrast to our findings.

Smaller NPs are believed to have the capability to diffuse through the gaps in the ECM between collagen fibrils. These gaps have been measured in the range of 20-40 nm in compact tumors, and up to 75-130 nm in poorly organized tumors [68]. An explanation for the poor diffusion of the smaller particles could be that the pore size in MCSs are more similar to healthy tumors than those of tumors. Contradictingly, Davies et. al (2002) found that the cell density of tumors where significantly higher than in the corresponding spheroid.

In general there was little NPs, for both sizes, that penetrated all the way to the core, and they mostly accumulated at the in the periphery. This can be due to attenuation of fluorescence from the core. The signal from the cells are still strong at this depth into the spheroid, but as the NPs are much smaller in size the signal of a single NP could be attenuated earlier than the other signals. The test to decide at what depth attenuation was lost was only done based on the CellTrace signals, not from the NPs. Hjelstuen et. al (1998) have reported attenuation affecting uptake measurements at depths larger than 60 µm, which is deeper into the spheroids than done in this study.

**Effect of NP surface-charge on uptake in MCSs**

Interestingly, as Tchoryk and her colleagues also tested the effect of surface charge on the uptake, it was revealed that for carboxylated (negatively charged) NPs the uptake was dramatically reduced [68]. While unmodified 50 nm NPs demonstrated the ability to penetrate deep into the spheroid ( 200 µm), their carboxylated counterparts only reached a distance equivalent to one cell diameter from the outer rim. This therefore explains the poor penetration to the core of the MCSs in our experiments, as the NPs used for the experiments in this thesis was the FluoSpheres Caroxulate-Modified Microspheres. The diameter of a tumor cells is known to be between 10-20 µm [69]. Accordingly, the intensity is for the most part accumulated at distances below 20 µm.

Lieleg et. al (2009) explained this to by electrostatic attraction and binding between the particles and charged areas in the ECM [70]. They described the ECM as a "hydrogel with local patches of either positive or negative charge", in which charged particles would be trapped in areas of the opposite charge. Neutral particles, on the other hand, could diffuse nearly unrestricted through the ECM. However, as the uptake experiments was conducted with negatively charged NPs, and the MCSs was found to be high in content of the negatively charged sGAGs [71], this contradicts the theory binding to opposite charged patches. Alternatively, the sGAG contents could lead to electrostatic repulsion instead of attraction, also ultimately reducing the uptake.

As a conclusion it seems that unmodified, neutral, NPs in the size range 30-50 nm would give the best therapeutic results of drug delivery. For this reason it would be of interest to repeat these NP uptake experiments with NPs of the same size with neutral surface charge to see if deeper penetration and higher accumulation of NPs in the core of the MCSs is obtained.

**Diffusion Through ECM vs Cellular Uptake**

Although not quantitatively confirmed, there seemed to be a significantly higher uptake of NPs into the TCs than in the fibroblasts. This can explain the overall higher uptake for CT26 MCSs, as there are more TCs on surface than for 4T1 MCSs. KPC MCSs also have a high number of TCs at the surface, however the overall uptake is much less than for CT26. This indicates a difference in cellular uptake, not only between TCs and fibroblasts, but also between different TCs.

Due to their larger size, NPs can not diffuse through the membrane of cells, but instead are expected to be taken up by the slower process of endocytosis [68]. Tchoryk et. al (2019) reports a high cellular uptake, but argues that the slow uptake process increases the probability of further penetration into the MCSs, as the diffusion process is able to compete with endocytosis. However in this study, as most particles are accumulated within the first cell layer, the cellular uptake seems to win over penetration.

Another hypothesis that can explain the low uptake and penetration through the areas high in fibroblasts, is the suggested electrostatic repulsion effect between the sGAG and the NPs. While no variation in sGAG contents was found between spheroid models, there was a significant difference in amounts of fibroblast in the periphery. As it is the fibroblasts that produce most ECM components, including sGAG, the fibroblast areas are expected to be higher in the negatively charged sGAGs. The difference in uptake could therefore be explained by a difference in sGAG positive areas on the surface of the MCSs, due to the difference in cellular organization. Collagen levels were found to be so low, that it would not have an effect on uptake. In general the correlation study between ECM and ECM contents can be neglected, due to low sample sizes. The most important result from the ECM experiments was that sGAG contents were found to be much higher than collagen.

It would however be interesting to be able to measure uptake and ECM content in the same spheroids, to get more insightful information about the correlation between ECM and uptake. With the current method it is only possible to get trends and average uptake/ECM contents, as the ECM assays require the collection of multiple MCSs to obtain measurable contents.

## 5.5 Future Work

As some of the most interesting findings from this study was regarding the difference in cellular organization and presumable cadherin-expression, an analysis to test the different cell lines for their cell adhesion and CAM expression is suggested. Cell-cell aggregation assays could be performed to quantitatively say something about the different levels of cell-cell adhesion in the different cell lines [22]. Altenatively, sectioning (i.e cryosectioning) of MCSs, followed by H&E (Haematoxylin and Eosin) staining is

a possible solution [36]. Cryosectioning would also be benefitial in order to measure ECM contents and NP uptake within the same spheroids, which could be acheived by two photon microscopy or second harmonic generation (SHG) [72]. In addition, sectioning of the MCSs would eliminate the potential problem of attenutation of signal from the core during NP uptake measurements. For the NP uptake experiments, it is also suggested to try neutral NPs instead of negatively charged particles, to see if this improves the penetration ability of the NPs into MCSs.

Furthermore, some improvements in the analysis of MCSs of low sphericity, like KPC MCSs, could be benefitial. A Matlab script similar to the one used in this study, only not using concentric circles, could be possible.

Lastly, a worthy mention is the recent research by Saemundsson et. al (2023) on a new method regarding DNA modification of cell interaction to produce uniform distribution of cell types within spheroids [60]. If it should be of interest to produce uniform spheroids with homogeneous cellular oganization, their method shows promising results.

# Chapter 6

# Conclusion

The objectives of this thesis were to characterize MCSs formed by coculturing three tumor cell lines, namely 4T1, CT26, and KPC, with ECM-producting fibroblasts, NIH/3T3. This involved examining the growth characteristics of the cells in both monolayer cultures and as MCSs. Furthermore, the thesis aimed to investigate the cellular organization, ECM contents, as well as NP uptake and penetration within the different MCSs.

An interesting finding was that all the three MCSs exhibited different cellular organization, which is thought to be due to cadherin-mediated cell segregation. They varied from homogeneous distribution of TCs and fibroblasts in CT26 MCSs, to a smaller segregation in 4T1 MCSs, and complete separation in KPC MCSs. These findings were supported by the inherent morphological differences observed in monolayer cultures, characterized by both epithelial (expressing E-cadherin) morphology and mesenchymal (expressing N-cadherin) phenotypes. Additionally, the spheroid models displayed variations in volume and sphericity, showing an inverse relationship with the extent of cell separation. Specifically, the CT26 MCSs were the largest with the highest sphericity, followed by the 4T1 MCSs, while the KPC MCSs were significantly smaller and less spherical. The same trend was also seen for average total NP uptake into the MCSs. No significant difference between ECM contents was found, hence it can not explain the difference in uptake. Alternatively, it is hypothesized that the cellular organization, in combination with potential differences in cellular uptake among the different cell lines, may contribute to these observed differences.

Going forward, it would be interesting to analyze the cadherin expression of the various cell lines to gain deeper insight into the mechanisms underlying their distinct cellular organizations. Moreover, conducting cryosectioning of the MCSs prior to analyzing NP uptake would eliminate potential signal attenuation while also enabling simultaneous measurements of collagen and NP uptake within the same spheroid.

# Appendix A

# Doubling times

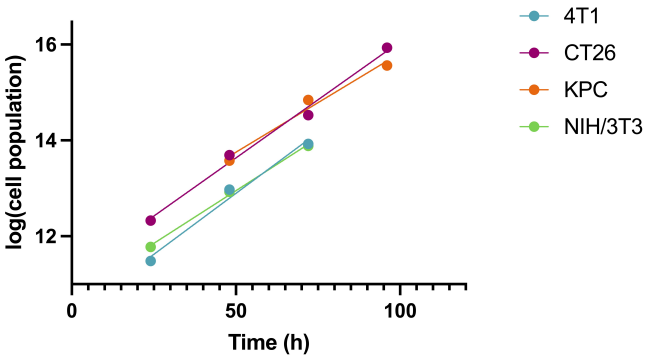


**Figure A.1:** Cell growth of cells in their in monolayer for tumor cell lines 4T1, CT26, KPC, as well as fibroblasts NIH/3T3. The data is only showed for the region in which the cells are in in the logarithmic phase of their growth phase.

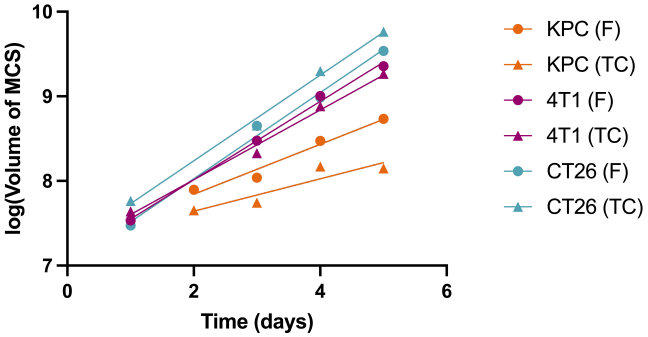


**Figure A.2:** Growth in volume of multicellular spheroids (MCSs) for tumor cell lines 4T1, CT26, KPC, in 1:5 ratio with fibroblasts NIH/3T3. Each spheroid models was grown in both growth medium optimal for the tumor cells (TC) of fibroblast (F). The data is only showed for the region in which the cells are in in the logarithmic phase of their growth phase.

# Appendix B

# Optimizing NP concentration

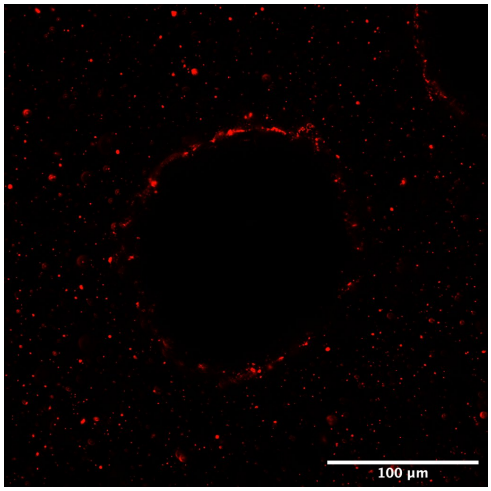


**(a)** NP concentration $0.25\,\mu L\,mL^{-1}$ after 3 hours incubation

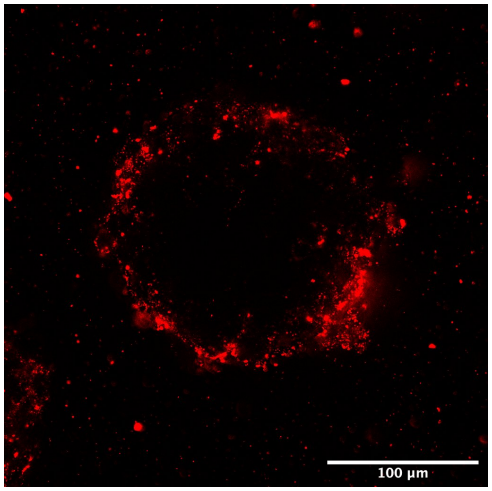


**(b)** NP concentration $0.25\,\mu L\,mL^{-1}$ after 24 hours incubation

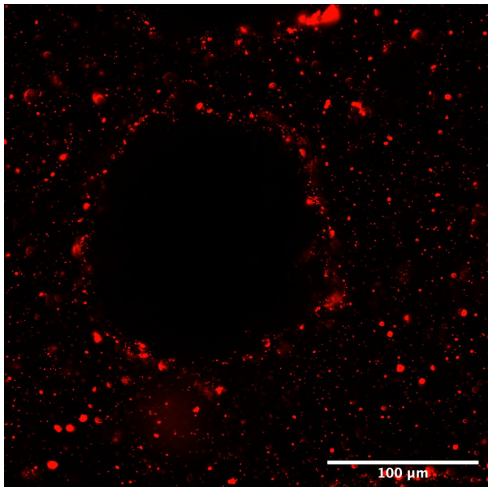


**(c)** NP concentration $1.25\,\mu L\,mL^{-1}$ after 3 hours incubation

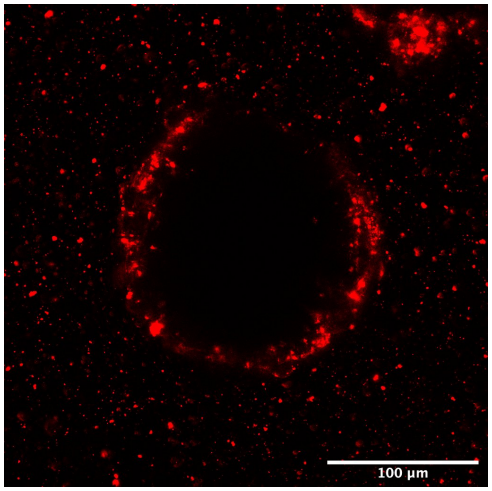


**(d)** NP concentration $1.25\,\mu L\,mL^{-1}$ after 24 hours incubation

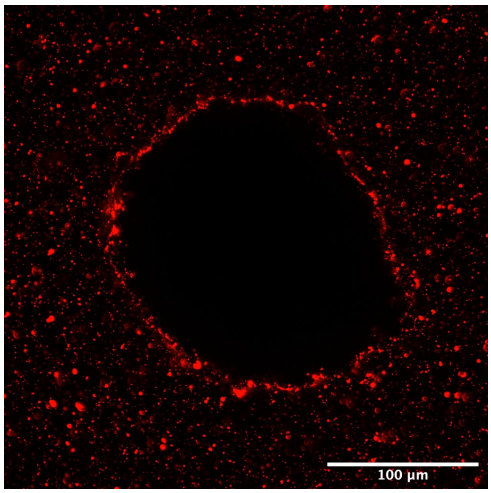


**(e)** NP concentration $2.5\,\mu L\,mL^{-1}$ after 3 hours incubation

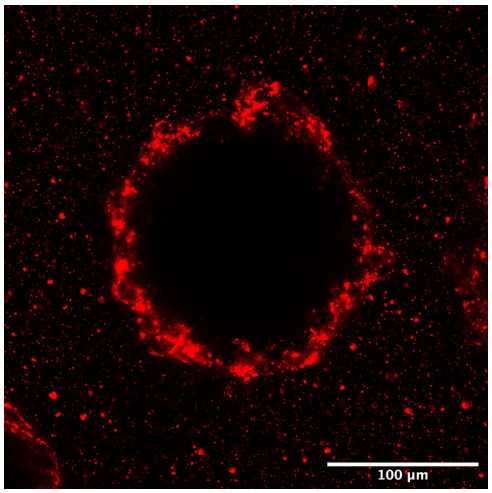


**(f)** NP concentration $2.5\,\mu L\,mL^{-1}$ after 24 hours incubation

# Bibliography


[1] H. Sung et al. 'Global Cancer Statistics 2020: GLOBOCAN Estimates of Incidence and Mortality Worldwide for 36 Cancers in 185 Countries'. In: *CA: A Cancer Journal for Clinicians* 71.3 (2021), pp. 209–249.

[2] K. A. Kurdziel et al. 'Human dosimetry and preliminary tumor distribution of 18F-fluoropaclitaxel in healthy volunteers and newly diagnosed breast cancer patients using PET/CT'. en. In: *J. Nucl. Med.* 52.9 (Sept. 2011), pp. 1339–1345.

[3] S. Roovers et al. 'Sonoprinting liposomes on tumor spheroids by microbubbles and ultrasound'. en. In: *J. Control. Release* 316 (Dec. 2019), pp. 79–92.

[4] K. Brunstøl. *Multicellular Spheroids as a Method for Drug Delivery Studies*. Specialization Project. NTNU, Dec. 2022.

[5] M. Janiszewska, M. C. Primi and T. Izard. 'Cell adhesion in cancer: Beyond the migration of single cells'. en. In: *J. Biol. Chem.* 295.8 (Feb. 2020), pp. 2495–2505.

[6] D. Hanahan and R. A. Weinberg. 'The hallmarks of cancer'. en. In: *Cell* 100.1 (Jan. 2000), pp. 57–70.

[7] D. Hanahan and R. A. Weinberg. 'Hallmarks of cancer: the next generation'. en. In: *Cell* 144.5 (Mar. 2011), pp. 646–674.

[8] R. Kalluri. 'The biology and function of fibroblasts in cancer'. en. In: *Nat. Rev. Cancer* 16.9 (Aug. 2016), pp. 582–598.

[9] R. Baghban et al. 'Tumor microenvironment complexity and therapeutic implications at a glance'. en. In: *Cell Commun. Signal.* 18.1 (Apr. 2020), p. 59.

[10] S. Pompili et al. 'The charming world of the extracellular matrix: A dynamic and protective network of the intestinal wall'. en. In: *Front. Med. (Lausanne)* 8 (Apr. 2021), p. 610189.

[11] P. Lu, V. M. Weaver and Z. Werb. 'The extracellular matrix: a dynamic niche in cancer progression'. en. In: *J. Cell Biol.* 196.4 (Feb. 2012), pp. 395–406.

[12] M. W. Pickup, J. K. Mouw and V. M. Weaver. 'The extracellular matrix modulates the hallmarks of cancer'. en. In: *EMBO Rep.* 15.12 (Dec. 2014), pp. 1243–1253.

[13] A. Derkacz et al. 'The diagnostic usefulness of circulating profile of extracellular matrix components: sulfated glycosaminoglycans (SGAG), hyaluronan (HA) and extracellular part of syndecan-1 (SCD138) in patients with Crohn's disease and ulcerative colitis'. In: *Journal of Clinical Medicine* 10.8 (2021), p. 1722.

[14] M. Nurmik et al. 'In search of definitions: Cancer-associated fibroblasts and their markers'. en. In: *Int. J. Cancer* 146.4 (Feb. 2020), pp. 895–905.

[15] Y. Zhao et al. 'Trajectory-based characteristic analysis and decision modeling of the lane-changing process in intertunnel weaving sections'. en. In: *PLoS One* 17.4 (Apr. 2022), e0266489.

[16] L. et al. *Molecular Cell Biology*. 2007.

[17] M. Maeda, K. R. Johnson and M. J. Wheelock. 'Cadherin switching: essential for behavioral but not morphological changes during an epithelium-to-mesenchyme transition'. In: *Journal of cell science* 118.5 (2005), pp. 873–887.

[18] E. Batlle et al. 'The transcription factor snail is a repressor of E-cadherin gene expression in epithelial tumour cells'. In: *Nature cell biology* 2.2 (2000), pp. 84–89.

[19] A. Cano et al. 'The transcription factor snail controls epithelial–mesenchymal transitions by repressing E-cadherin expression'. In: *Nature cell biology* 2.2 (2000), pp. 76–83.

[20] M. T. Nieman et al. 'N-cadherin promotes motility in human breast cancer cells regardless of their E-cadherin expression'. In: *The Journal of cell biology* 147.3 (1999), pp. 631–644.

[21] R. B. Hazan et al. 'Exogenous expression of N-cadherin in breast cancer cells induces cell migration, invasion, and metastasis'. In: *The Journal of cell biology* 148.4 (2000), pp. 779–790.

[22] R. B. Hazan et al. 'N-cadherin promotes adhesion between invasive breast cancer cells and the stroma'. In: *Cell adhesion and communication* 4.6 (1997), pp. 399–411.

[23] A. L. Berrier and K. M. Yamada. 'Cell–matrix adhesion'. In: *Journal of Cellular Physiology* 213.3 (2007), pp. 565–573. DOI: https://doi.org/10.1002/jcp.21237. eprint: https://onlinelibrary.wiley.com/doi/pdf/10.1002/jcp.21237. URL: https://onlinelibrary.wiley.com/doi/abs/10.1002/jcp.21237.

[24] G. Liu et al. 'A Review on drug delivery system for tumor therapy'. In: *Frontiers in Pharmacology* 12 (2021), p. 735446.

[25] B. Haley and E. Frenkel. 'Nanoparticles for drug delivery in cancer treatment'. en. In: *Urol. Oncol.* 26.1 (Jan. 2008), pp. 57–64.

[26] S. Ashique et al. 'Targeted drug delivery: Trends and perspectives'. en. In: *Curr. Drug Deliv.* 18.10 (2021), pp. 1435–1455.

[27] R. Rasouli, R. A. Paun and M. Tabrizian. 'Sonoprinting nanoparticles on cellular spheroids via surface acoustic waves for enhanced nanotherapeutics delivery'. en. In: *Lab Chip* 23.8 (Apr. 2023), pp. 2091–2105.

[28] J. W. Shreffler et al. 'Overcoming hurdles in nanoparticle clinical translation: The influence of experimental design and surface modification'. In: *International journal of molecular sciences* 20.23 (2019), p. 6056.

[29] R. K. Jain. 'Vascular and interstitial barriers to delivery of therapeutic agents in tumors'. In: *Cancer Metastasis Rev* 9.3 (Nov. 1990), pp. 253–266.

[30] A. K. Iyer et al. 'Exploiting the enhanced permeability and retention effect for tumor targeting'. en. In: *Drug Discov. Today* 11.17-18 (Sept. 2006), pp. 812–818.

[31] Z. Li et al. 'Application of animal models in cancer research: Recent progress and future prospects'. en. In: *Cancer Manag. Res.* 13 (Mar. 2021), pp. 2455–2475.

[32] O. Graudejus et al. 'Bridging the gap between in vivo and in vitro research: Reproducing in vitro the mechanical and electrical environment of cells in vivo'. In: *Frontiers in Cellular Neuroscience* 12 (2018).

[33] O. Habanjar et al. '3D cell culture systems: Tumor application, advantages, and disadvantages'. en. In: *Int. J. Mol. Sci.* 22.22 (Nov. 2021), p. 12200.

[34] *Bridging the gap between three-dimensional cultures and animal models.* [Online; accessed 14-December-2022]. Sept. 2022. URL: https://facellitate.com/bridging-the-gap-between-three-dimensional-cultures-and-animal-models/.

[35] R. M. Sutherland et al. 'A multi-component radiation survival curve using an in vitro tumour model'. In: *International Journal of Radiation Biology and Related Studies in Physics, Chemistry and Medicine* 18.5 (1970), pp. 491–495.

[36] M. L. Lotsberg et al. 'Intrinsic differences in spatiotemporal organization and stromal cell interactions between isogenic lung cancer cells of epithelial and mesenchymal phenotypes revealed by high-dimensional single-cell analysis of heterotypic 3D spheroid models'. In: *Frontiers in Oncology* 12 (2022).

[37] A. Alghuwainem, A. T. Alshareeda and B. Alsowayan. 'Scaffold-free 3-D cell sheet technique bridges the gap between 2-D cell culture and animal models'. en. In: *Int. J. Mol. Sci.* 20.19 (Oct. 2019), p. 4926.

[38] X. Cui, Y. Hartanto and H. Zhang. 'Advances in multicellular spheroids formation'. en. In: *J. R. Soc. Interface* 14.127 (Feb. 2017).

[39] T.-M. Achilli, J. Meyer and J. R. Morgan. 'Advances in the formation, use and understanding of multi-cellular spheroids'. In: *Expert opinion on biological therapy* 12.10 (2012), pp. 1347–1360.

[40] R. M. Enmon Jr et al. 'Dynamics of spheroid self-assembly in liquid-overlay culture of DU 145 human prostate cancer cells'. In: *Biotechnology and bioengineering* 72.6 (2001), pp. 579–591.

[41] D. M. Dean et al. 'Rods, tori, and honeycombs: the directed self-assembly of microtissues with prescribed microscale geometries'. In: *The FASEB Journal* 21.14 (2007), pp. 4005–4012.

[42] T. Nederman et al. 'Demonstration of an extracellular matrix in multicellular tumor spheroids'. en. In: *Cancer Res.* 44.7 (July 1984), pp. 3090–3097.

[43] B. H. Lee et al. 'Modulation of Huh7.5 spheroid formation and functionality using modified PEG-based hydrogels of different stiffness'. en. In: *PLoS One* 10.2 (Feb. 2015), e0118123.

[44] A. García-Herraiz et al. 'Applications of Confocal Laser Scanning Microscopy in Dentistry. Study of the changes of the post-extraction sites.' In: 2012.

[45] S. Shah et al. 'Predicting porosity and permeability of carbonate rocks from core-scale to pore-scale using medical CT, confocal laser scanning microscopy and micro CT'. In: *SPE Annual Technical Conference and Exhibition?* SPE. 2013.

[46] W. Mäntele and E. Deniz. 'UV-VIS absorption spectroscopy: Lambert-Beer reloaded'. en. In: *Spectrochim. Acta A Mol. Biomol. Spectrosc.* 173 (Feb. 2017), pp. 965–968.

[47] D. L. Priwitaningrum et al. 'Tumor stroma-containing 3D spheroid arrays: A tool to study nanoparticle penetration'. In: *Journal of controlled release* 244 (2016), pp. 257–268.

[48] *Thermo Fisher Scientific: C34557 Product Page*. Online. Accessed: April 23, 2023. URL: https://www.thermofisher.com/order/catalog/product/C34557.

[49] H. F. Wesche. *Characterization of extracellular matrix constituents in three murine tumor models*. Specialization Project. NTNU, Feb. 2023.

[50] Biocolor Ltd. *Sircol™ - Soluble Collagen assay kit*. Online. Accessed: May 12, 2023. 2022. URL: https://www.biocolor.co.uk/ecm-assays/sircol-soluble-collagen-assay.

[51] Biocolor Ltd. *Blyscan™ - sulfated Glycosaminoglycan (sGAG) assay kit*. Online. Accessed: May 12, 2023. 2022. URL: https://www.biocolor.co.uk/ecm-assays/blyscan-glycosaminoglycan-assay.

[52] *4T1*. [Online; accessed 18-December-2022]. URL: https://www.atcc.org/products/crl-2539.

[53] G. L. Dobek et al. 'Analysis of promoters and expression-targeted gene therapy optimization based on doubling time and transfectability'. en. In: *FASEB J.* 25.9 (Sept. 2011), pp. 3219–3228.

[54] *NIH-3T3*. [Online; accessed 18-December-2022]. URL: https://www.dsmz.de/collection/catalogue/details/culture/ACC-59.

[55] *CT26.WT*. [Online; accessed 18-December-2022]. URL: https://www.atcc.org/products/crl-2638.

[56] A. Li et al. 'Fascin is regulated by slug, promotes progression of pancreatic cancer in mice, and is associated with patient outcomes'. In: *Gastroenterology* 146.5 (2014), pp. 1386–1396.

[57] Y. Lou et al. 'Epithelial–mesenchymal transition (EMT) is not sufficient for spontaneous murine breast cancer metastasis'. In: *Developmental Dynamics* 237.10 (2008), pp. 2755–2768.

[58] A. Alharthi et al. 'Distinct effects of pharmacological inhibition of stromelysin1 on endothelial-to-mesenchymal transition and myofibroblast differentiation'. In: *Journal of cellular physiology* 236.7 (2021), pp. 5147–5161.

[59] J. C. Castle et al. 'Immunomic, genomic and transcriptomic characterization of CT26 colorectal carcinoma'. en. In: *BMC Genomics* 15 (Mar. 2014), p. 190.

[60] S. A. Saemundsson et al. 'Controlling Cell Organization in 3D Coculture Spheroids Using DNA Interactions'. In: *ACS Biomaterials Science & Engineering* (2023).

[61] M. S. Steinberg and M. Takeichi. 'Experimental specification of cell sorting, tissue spreading, and specific spatial patterning by quantitative differences in cadherin expression.' In: *Proceedings of the National Academy of Sciences* 91.1 (1994), pp. 206–209.

[62] C. Davies et al. 'Comparison of extracellular matrix in human osteosarcomas and melanomas growing as xenografts, multicellular spheroids, and monolayer cultures.' In: *Anticancer research* 17.6D (1997), pp. 4317–4326.

[63] D. R. Grimes et al. 'The role of oxygen in avascular tumor growth'. In: *PloS one* 11.4 (2016), e0153692.

[64] G. Alzeeb et al. 'Gastric cancer cell death analyzed by live cell imaging of spheroids'. In: *Scientific reports* 12.1 (2022), p. 1488.

[65] *Sodium Pyruvate (100 mM)*. [Online; accessed 26-June-2023]. URL: https://www.thermofisher.com/order/catalog/product/11360070.

[66] R. V. Iozzo. 'Proteoglycans and neoplasia'. In: *Cancer and Metastasis Reviews* 7 (1988), pp. 39–50.

[67] C. Davies et al. 'Comparison of IgG diffusion and extracellular matrix composition in rhabdomyosarcomas grown in mice versus in vitro as spheroids reveals the role of host stromal cells'. In: *British journal of cancer* 86.10 (2002), pp. 1639–1644.

[68] A. Tchoryk et al. 'Penetration and uptake of nanoparticles in 3D tumor spheroids'. In: *Bioconjugate Chemistry* 30.5 (2019), pp. 1371–1384.

[69] B. Shashni et al. 'Size-based differentiation of cancer and normal cells by a particle size analyzer assisted by a cell-recognition PC software'. In: *Biological and Pharmaceutical Bulletin* 41.4 (2018), pp. 487–503.

[70] O. Lieleg, R. M. Baumgärtel and A. R. Bausch. 'Selective filtering of particles by the extracellular matrix: an electrostatic bandpass'. In: *Biophysical journal* 97.6 (2009), pp. 1569–1577.

[71] S. De Bruin et al. 'Sulfated glycosaminoglycan-like polymers are present in an acidophilic biofilm from a sulfidic cave'. In: *Science of the Total Environment* 829 (2022), p. 154472.

[72] I. A. Khawar et al. 'Three dimensional mixed-cell spheroids mimic stroma-mediated chemoresistance and invasive migration in hepatocellular carcinoma'. In: *Neoplasia* 20.8 (2018), pp. 800–812.

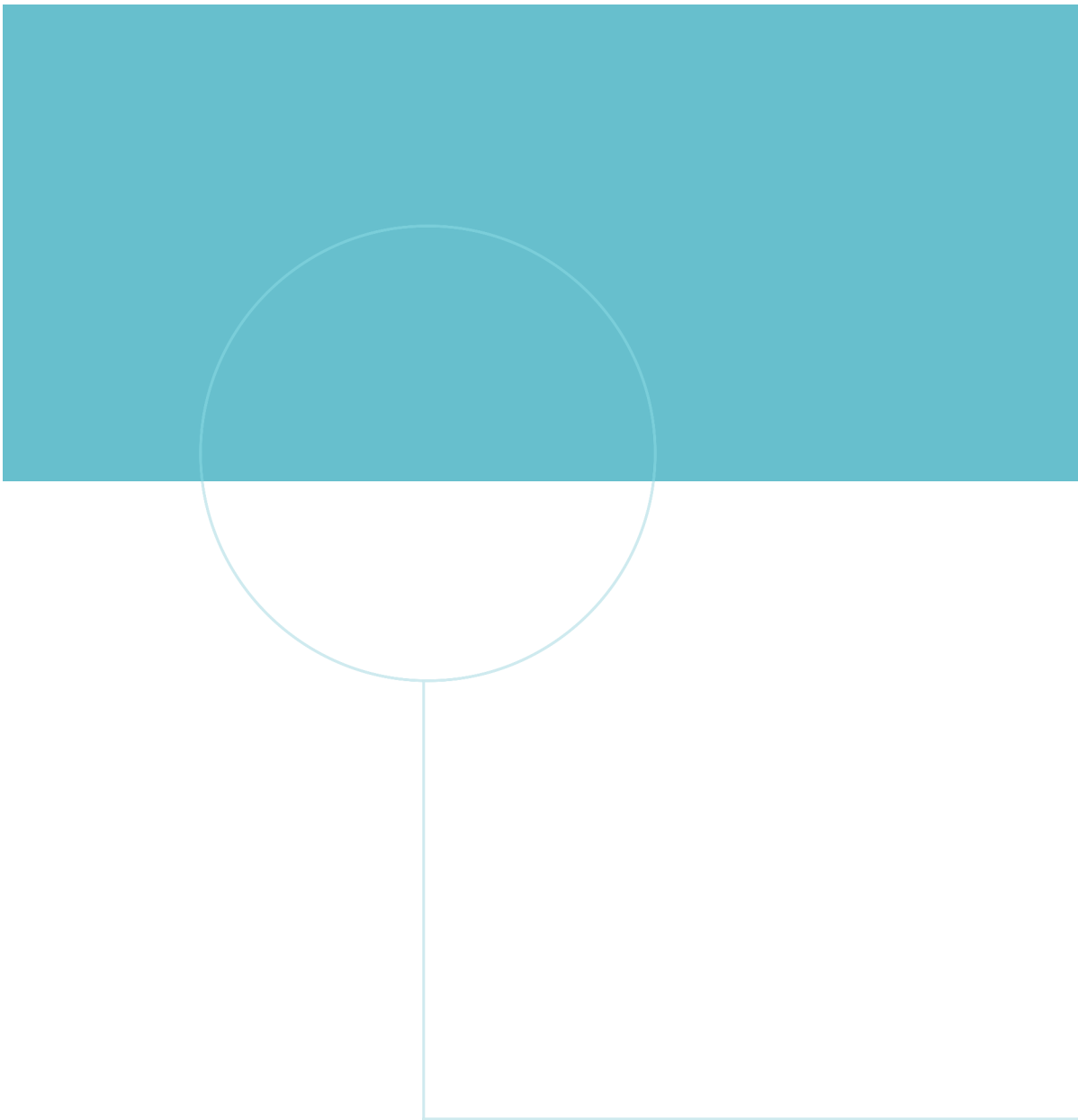

NTNU

Norwegian University of
Science and Technology